Electrical conductivity of the Lithosphere-Asthenosphere System

Samer Naif, Kate Selway, Benjamin S. Murphy, Gary Egbert, Anne Pommier

1. Introduction

Electromagnetic geophysical methods image the electrical conductivity of the subsurface. Electrical conductivity is an intrinsic material property that is sensitive to temperature, composition, porosity, volatile and/or melt content, and other physical properties relevant to the solid Earth. Therefore, imaging the electrical structure of the crust and mantle yields valuable information on the physical and chemical state of the lithosphere-asthenosphere system.

Here we explore the viability of the passive magnetotelluric (MT) method for constraining upper mantle properties. We approach this problem in four successive steps: 1) review the electrical conductivity behavior of relevant materials; 2) predict the bulk electrical conductivity structure of oceanic and continental lithosphere for a suite of representative physical states; 3) generate synthetic MT data from the conductivity predictions; 4) compare and discuss the conductivity predictions and the synthetic data with select case studies from oceanic and continental settings. Our aim is to clarify the uncertainties associated with drawing inferences from electrical conductivity observations and ultimately to provide a basis for assigning confidence levels to interpretations.

2. Electrical conductivity of Earth's materials

Electrical conductivity (EC) is a measure of a material's ability to conduct electric current and has SI units of siemens per meter [S/m]. It is the reciprocal of electrical resistivity—a material's ability to resist the flow of electric current (SI units of ohm-meters, [Ω·m]). Throughout this review, we frequently switch between referring to conductivity and resistivity. Most of the equations use EC units (Section 3 on the MT method is the exception). However, we stick to the convention of quoting the resistivity values in order to make direct comparisons with the MT data in later sections.

The EC of a material is governed by the net flux of charge carriers, which may consist of multiple carrier species each acting as a separate conduction mechanism

$$\sigma_i = c_i q_i \mu_i \tag{1}$$

where the index i denotes the ith species, σ_i is the EC due to the flux of the ith species, c_i is its charge concentration, q_i is its effective particle charge, and μ_i is its charge carrier mobility. The EC of a material is the cumulative sum of all conduction mechanisms operating, although it is common for a single mechanism to dominate for a given thermal regime.

In electrolyte solutions and semiconductors, the flux of charge carriers is physically related to a diffusion process, per Einstein's relation describing Brownian motion

$$D_i = \frac{\mu_i k_B T}{q_i} \tag{2}$$

where D_i is the diffusivity of the ith species, k_B is the Boltzmann's constant, and T is the absolute temperature. Rearranging Eq. 2 and substituting into Eq. 1 yields the Nernst-Einstein relation

$$\sigma_i = \frac{D_i c_i {q_i}^2}{k_B T} \tag{3}$$

which is an expression that can be used to predict the EC of a particular charge carrier species i from its self-diffusivity and vice versa (e.g., Mott & Gurney, 1948; Misener, 1974; Karato, 1990).

Three major categories describe the electrical behavior of materials: insulators, semiconductors, and conductors. For example, at ambient pressure-temperature (P-T) conditions, graphite is a conductor ($\sim 10^{-5}$ Ω·m) and quartz is an insulator ($\sim 10^{15}$ Ω·m) (e.g., Tyburczy & Fisler, 1995). The pair are electrical endmembers that differ by a staggering 20 orders of magnitude. Yet the majority of naturally occurring minerals in Earth's crust and mantle are semiconductors that exhibit overlapping EC values (Fig 1). More importantly, the crust and mantle are compositionally heterogeneous while electromagnetic (EM) soundings provide a bulk measurement of EC that represents a volume average of the aggregate of constituent materials. Secondary phases such as metal oxides/sulfides, aqueous solutions, and molten silicates can be several orders of magnitude more conductive than their host rock. As a result, the bulk EC may be controlled by small amounts of highly conductive materials when they form interconnected networks. Indeed, nearly all EM observations of the crust and upper mantle are confined to a relatively narrow band of 0.1–10^6 Ω·m. Note that in the specific case of the MT method, the absence of highly resistive anomalies greater than $\sim 10^4$ Ω·m is due to a lack of data sensitivity to insulators (see Section 4.1.1). It is therefore crucial to consider the ambiguity inherent in inferring the physical state from EC observations even in the case of perfectly known subsurface electric structure.

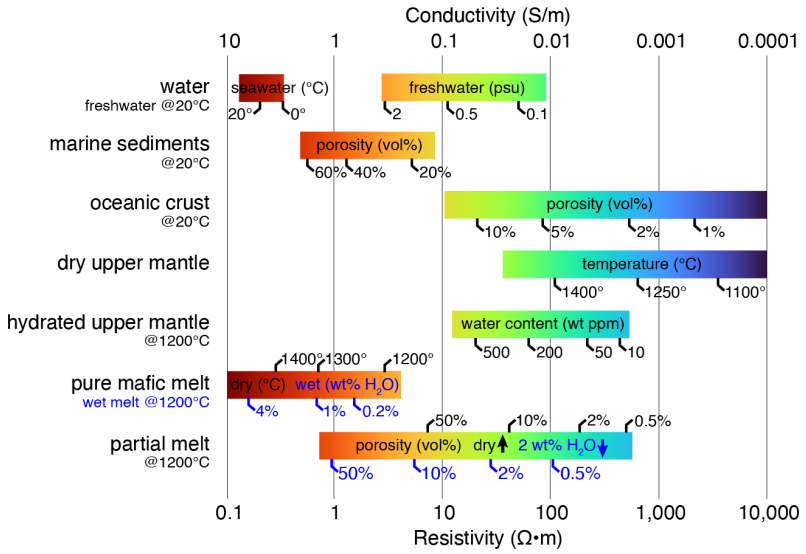

Figure 1: *The electrical conductivity (EC) of representative Earth materials. Freshwater EC is calculated at 20 ℃ as a function of practical salinity units (psu); seawater is 35 psu and drinking water is <0.5 psu. Marine sediment and oceanic crust EC are calculated with 20 ℃ seawater. Hydrated upper mantle EC is calculated at 1200 ℃ as a function of water content. Mafic melt EC is calculated as a function of temperature for anhydrous melt (black) and as a function of water content at 1200 ℃ for hydrous melt (blue). Partial melt EC is calculated at 1200 ℃ as a function of porosity for anhydrous (black) and hydrous mafic melt with 2 wt% water (blue). See Section 2 for details. Colorbar shows typical scale used to plot MT inversion.*

2.1 Conduction in solids

Naturally occurring crystalline materials, including silicate minerals, are predominantly semiconductors that host charge carriers in the form of intrinsic point defects and extrinsic impurities in the crystal lattice. Since the mobility of charge carriers is thermally activated, the EC is proportional to temperature and can be described in the form of an Arrhenius equation (Arrhenius, 1889)

$$\sigma = \sum_i \sigma_{0,i} \exp\left(-\frac{\Delta E_i}{k_B T}\right) \tag{4}$$

where $\sigma_{0,i}$ is the pre-exponential factor of the ith species and ΔE_i is its activation energy. Note that since the Nernst-Einstein relation (Eq. 3) is a function of the diffusivity, it also has the exponential behavior seen in Eq. 4 since the diffusivity itself depends on the mobility (per Eq. 2). Furthermore, in addition to the mobility, the concentration of charge carriers can also be a thermally activated quantity. The EC of a material is also sensitive to pressure, in which case the activation enthalpy is a more meaningful quantity than activation energy

$$\Delta H = \Delta E + P\Delta V \tag{5}$$

where ΔH is the activation enthalpy, P is the pressure, and ΔV is the activation volume. A positive activation volume will reduce the EC with increasing pressure.

The mantle is predominantly composed of ferromagnesian silicate minerals, all nominally anhydrous minerals (NAMs). The upper mantle commonly has modal proportions of 50–90% olivine, 10–40% pyroxene, and 0–20% garnet (e.g., Griffin et al., 2009). Although a variety of point defect populations exist in ferromagnesian NAMs (e.g., Smyth & Stocker, 1975), only three are considered to be important conduction mechanisms in the upper mantle (e.g., Schock & Duba, 1985)

$$\sigma = \sigma_{\mathrm{Mg}} + \sigma_{\mathrm{Fe}} + \sigma_{\mathrm{H}} \tag{6}$$

where subscript 'Mg' represents magnesium vacancy diffusion (ionic conduction), subscript 'Fe' represents electron exchange between ferric and ferrous iron (small polaron hopping), and subscript 'H' represents hydrogen diffusion in water-bearing minerals (proton conduction) (see Yoshino (2010) for schematic diagrams of all three conduction mechanisms). Because pressure typically has a small effect on EC relative to temperature (e.g., Xu et al., 2000), it is not uncommon in the literature to implicitly assume $\Delta V = 0$ and thereby assume ΔE to mean ΔH (e.g., Gardés et al., 2014). However, constraining the effect of pressure on EC is important to develop accurate electrical models that span large pressure (depth) ranges, particularly at higher temperatures prevalent in the asthenosphere where the conduction mechanism expected to dominate for that thermal regime (σ_{Mg}) may have a significant activation volume in olivine (e.g., Yoshino et al., 2017; Fei et al., 2018; 2020).

2.1.1 Anhydrous conduction

A prominent thermally activated conduction mechanism is the creation and migration of ionic vacancies in the crystal lattice. The most relevant intrinsic charge carriers in upper mantle NAMs are magnesium cation vacancies. Their contribution to conductivity is approximated by

$$\sigma_{\mathrm{Mg}} = \sigma_{0,\mathrm{Mg}} \exp\left(-\frac{\Delta H_{\mathrm{Mg}}}{k_B T}\right) \tag{7}$$

where the pre-exponential factor $\sigma_{0,\mathrm{Mg}}$ is a constant.

Another prominent conduction mechanism in iron-bearing NAMs is small polaron hopping. Electronic conduction via small polaron hopping is a byproduct of iron substituting for magnesium at a cation site. Iron can take on the form of either a ferrous (Fe^{2+}) or ferric (Fe^{3+}) ion. The excess positive charge in Fe^{3+} is a result of an electron hole, and it is the transfer (or "hopping") of electron holes between Fe^{3+} and Fe^{2+} that is responsible for the conduction (Hirsch et al., 1993). The hopping flux—and hence its contribution to EC—peaks when the proportions of Fe^{3+} and Fe^{2+} are equivalent.

At a fixed composition, the speciation of iron is indicative of the in situ oxygen fugacity and is governed by thermodynamics (see Frost (1991) for an introduction to oxygen fugacity). Although some amount of Fe^{3+} is present in NAMs at the oxygen fugacity and temperature conditions prevalent in the upper mantle, Fe^{2+} is much more abundant in these minerals because it substitutes a divalent magnesium (Mg^{2+}) in an Mg site and maintains charge neutrality (Yoshino, 2010). Hence, the concentration of Fe^{3+} is the limiting agent in small polaron conduction. Since the proportion of Fe^{3+} tends to increase with increasing oxygen fugacity, the flux of small polaron charge carriers depends on both the total iron content and the oxygen fugacity

$$\sigma_{\mathrm{Fe}} = \sigma_{0,\mathrm{Fe}} X_{\mathrm{Fe}} f_{\mathrm{O}_2}^{q} \exp\left(-\frac{\Delta H_{\mathrm{Fe}}}{k_B T}\right) \tag{8}$$

where X_{Fe} is the mole fraction of iron, f_{O_2} is the oxygen fugacity, and exponent q is a constant. Several studies have noted that an increasing iron content reduces the Fe^{2+}–Fe^{3+} hopping distance, which should reduce the activation enthalpy (e.g., Seifert et al., 1982; Romano et al., 2006). Yoshino & Katsura (2009) proposed using an n-type semiconductor model to approximate the effect of iron content on the activation enthalpy

$$\Delta H_{\mathrm{Fe}} = \Delta H_{0,\mathrm{Fe}} - \alpha_{\mathrm{Fe}} X_{\mathrm{Fe}}^{1/3} \tag{9}$$

where $\Delta H_{0,\mathrm{Fe}}$ is the activation enthalpy at diminishing iron content and α_{Fe} is a constant.

On average, the upper mantle is thought to have an oxygen fugacity that falls within a few log units of the quartz-fayalite-magnetite (QFM) buffer as well as a relatively fixed iron content of $X_{\mathrm{Fe}} \approx 0.09$–$0.11$ (Frost & McMammon, 2008). By treating both X_{Fe} and f_{O_2} as constants, we can incorporate both terms into the pre-exponential factor $\sigma_{0,\mathrm{Fe}}$ and simplify Eq. 8 into

$$\sigma_{\mathrm{Fe}} = \sigma_{0,\mathrm{Fe}} \exp\left(-\frac{\Delta H_{\mathrm{Fe}}}{k_B T}\right) \tag{10}$$

In the absence of hydration, holding the iron content and oxygen fugacity fixed implies that temperature alone controls mantle conductivity since it is the only remaining free variable in Eq. 7 and Eq. 10. In NAMs, small polaron hopping is likely the dominant conduction mechanism in anhydrous upper mantle for colder temperatures (<1300°C) since it has a lower activation enthalpy (ΔE_{Fe}~1.3–1.7 eV) than magnesium vacancy diffusion (ΔE_{Mg}>2 eV) (Schock et al., 1989; Hirsch et al., 1993; Constable & Roberts, 1997).

2.1.2 Hydrous conduction

Hydrogen is an extrinsic ionic impurity and one of the fastest diffusing charge carriers in NAMs (Kohlstedt & Mackwell, 1998; Ferriss et al., 2016; Reynes et al., 2018). Based on the Nernst-Einstein relation (Eq. 3), hydrogen is predicted to enhance EC due to its high mobility (Karato, 1990). Indeed, a growing body of experimental studies have all confirmed a significant EC enhancement for hydrogen-doped NAMs (e.g., Wang et al., 2006; Yoshino et

al., 2006; 2009; Poe et al., 2010; Dai & Karato, 2014; Dai et al., 2020). Therefore, since hydrogen (commonly referred to as "water") is prevalent in the mantle at regionally variable concentrations (e.g., Li et al., 2008; Kelley et al., 2019), EC observations provide a means to infer bulk mantle water content.

Two distinct forms of the Arrhenius equation have been proposed to account for the effect of hydrogen on EC. The first employs the *n*-type semiconductor model seen in Eq. 9, but in this case considers the effect of hydrogen content on activation enthalpy (Yoshino et al., 2009)

$$\sigma_{\mathrm{H}} = \sigma_{0,\mathrm{H}} C_{\mathrm{w}} \exp\left(-\frac{\Delta H_{\mathrm{H}} - \alpha C_{\mathrm{w}}^{1/3}}{k_B T}\right) \tag{11}$$

where C_{w} is the water content in wt%. In contrast, the second form assumes no activation enthalpy dependence on total water content and instead considers hydrogen speciation, or the mechanism by which hydrogen is incorporated into the crystal lattice and enhances conductivity (Wang et al., 2006)

$$\sigma_{\mathrm{H}} = \sigma_{0,\mathrm{H}} C_{\mathrm{w}}^{r} \exp\left(-\frac{\Delta H_{\mathrm{H}}}{k_B T}\right) \tag{12}$$

where the exponent r is a constant whose value depends on the hydrogen speciation. When $r = 1$, all of the hydrogen protons are incorporated and contributing to EC. In this scenario, the EC value determined from in situ measurements would match the EC value predicted by the Nernst-Einstein relation (Eq. 3), since the latter is calculated using the self-diffusivity and total concentration of hydrogen.

Regardless of which Arrhenius form is applied (Eq. 11 or Eq. 12) and/or the origin of the conduction mechanism, there are significant discrepancies between the in situ EC measurements on hydrated olivine from independent laboratory groups (e.g., Yoshino & Katsura, 2013; Karato, 2013; Gardés et al., 2014; and references cited in Fig 2). Yet another noteworthy discrepancy is in the activation enthalpy (ΔH_{H}) of olivine determined from in situ EC (~0.9 eV) and isotope diffusion measurements (~1.3–2.1 eV; Du Frane & Tyburczy, 2012; Novella et al., 2017; Sun et al., 2019), which is a source of ongoing debate on whether this reflects distinct isotope diffusion and electrical conduction mechanisms and, hence, the validity of applying the Nernst-Einstein relation to predict the EC for hydrated olivine (e.g., Karato, 2013; 2015; Jones, 2016; Sun et al., 2019). In practice, these discrepancies hinder attempts to infer precisely the concentration of mantle water from MT observations. To illustrate this, Figure 2a shows the EC predictions as a function of water content from several competing olivine models at 1200°C. For 100 Ω·m mantle, the water content estimates vary by two orders of magnitude (7–800 ppm H_2O). This uncertainty is significantly reduced, to about half an order of magnitude (60–300 ppm H_2O), when only the most recent model from each laboratory group is considered (in effect excluding W06 and Y09). It is not

unreasonable to assume that this uncertainty reduction is in part due to technical advancements that allow more accurate EC measurements for hydrous minerals. Therefore, our hydrous mantle EC calculations in Section 4, which adopt W06 and Y09, represent a 'worst-case' scenario and potentially overstate this uncertainty.

Relatively few experimental studies have investigated the EC of other NAMs under hydrous conditions. Competing models for pyrope-rich garnet (Dai & Karato, 2009a; Dai et al., 2012) and orthopyroxene (Dai & Karato, 2009b; Schlechter et al., 2012; Zhang et al., 2012) also show large EC differences (Fig 2b). This is particularly so for garnet, since the D09a model is significantly more conductive than all of the NAM models considered here. Dai et al. (2012) measured the EC of a garnet sample of identical chemical composition to that used in D09a and, as expected, the results are equivalent under dry conditions. However, at 465 ppm H_2O (the only water content considered), the results are around seven times less conductive than D09a. Since Dai et al. (2012) did not give an empirical model for garnet EC as a function of water content, we provide one here based on the Dai & Karato (2014) formulation for olivine, which also only measured EC at a single hydration level

$$\sigma_{\mathrm{H}} = \sigma_0 \left(\frac{C_{\mathrm{w}}}{C_{\mathrm{w},0}} \right)^r \exp\left(-\frac{\Delta H}{k_B T} \right) \tag{13}$$

where $C_{\mathrm{w},0}$ is the water content at the reference state (465 ppm in this case) and $r = 0.63$ per D09a. The resulting model (D12), shown in Fig 2b, has similar behavior to D09a except that it is more resistive.

The source(s) of the experimental disagreement remains unclear, although possible culprits include inaccurate water content measurements, sample dehydration during experimental runs, grain boundary effects in polycrystalline samples, and/or nonuniform hydration or chemical zonation of the starting sample (e.g., Gardés et al., 2014; Jones, 2016). The largest potential source of error is likely water content measurements using Fourier Transform Infrared (FTIR) spectroscopy. Conductivity studies that use unpolarized light often apply the Paterson (1982) calibration to determine the water content, but this approach is prone to introducing nonsystematic errors (Libowitzky & Rossman, 1996) and has been shown to underestimate water in NAMs by as much as a factor of 3–3.5 (Bell et al., 1995; 2003). This has significant implications for the EC models of hydrous minerals and has been proposed as an explanation for the lab discrepancies (Poe et al., 2010; Gardés et al., 2014). Unfortunately, recalibrating unpolarized FTIR measurements is nonlinear and requires sample-specific details in addition to the raw spectra, which were not documented in prior studies. Therefore, throughout this review, we use the EC models in their original form without applying any corrections. This is likely to mean that we are overestimating the effect of hydration on mantle conductivity, and as such our hydrous mantle EC models should be considered upper bound estimates (Naif, 2018). We encourage future experimental studies

to document the necessary details that allow applying newer and more accurate calibrations as they become available.

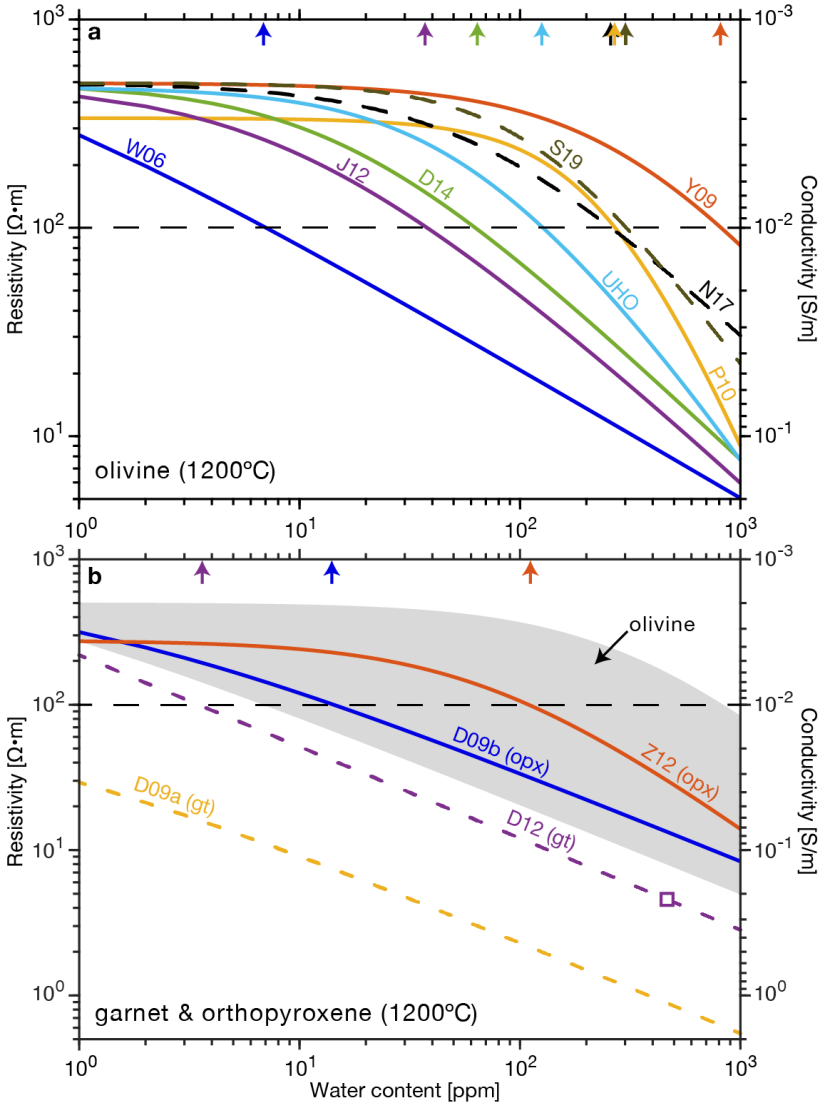

Figure 2: *Electrical conductivity of NAMs as a function of water content at 1200°C. (**a**) EC models for olivine [W06–Wang et al., 2006; Y09–Yoshino et al., 2009; P10–Poe et al., 2010; J12–Jones et al., 2012; D14–Dai & Karato, 2014; UHO–Gardés et al., 2014; N17–Novella et al., 2017; S19–Sun et al., 2019]. The solid lines are models from in situ EC measurements and dashed lines from isotope self-diffusion measurements. The colored arrows mark the water content at 100 Ω·m from each model, which ranges between 7 and 800 ppm H_2O. (**b**) EC models for pyrope-rich garnet [D09a–Dai & Karato, 2009a; D12–Dai et al., 2012] and orthoenstatite [D09b–Dai & Karato, 2009b; Z12–Zhang et al., 2012]. The D12 model for garnet is our extrapolation from that study's measurement at a single water content (465 ppm), shown by the purple square (see Eq. 13 and text for details). The grey region shows the range of olivine EC values from the models in (**a**). Note that all of the model curves in both panels are extrapolations since the experiments were limited to 1000 ℃ or less (1100 ℃ for D14) to avoid sample dehydration.*

2.2 Conduction in fluids

Although the hydrogen conduction mechanisms are debated for some silicate minerals, ionic diffusion is almost always the primary control on EC for liquids due to the abundance and high diffusivity of ionic charge carriers in solution. This is true for silicate and carbonate melts as well as aqueous solutions consisting of salts dissolved in water.

2.2.1 Aqueous solutions

The EC of an aqueous solution is governed by the concentration of ions and their respective mobilities, as per Eq. 1 and Eq. 3. The contribution of a particular solute to the EC depends on the degree to which it dissociates to form free ions when dissolved in water. Furthermore, because the solubility, degree of dissociation, and mobility of a solute all have a nonlinear dependence on the thermodynamic state, the EC behavior of a solution under varying P-T conditions is complex.

Pure water consists of H_2O molecules in equilibrium with a very small quantity of dissociated H^+ and OH^- ions that are highly mobile. It has a resistivity on the order of 10^5 Ω·m at ambient P-T (1 atm, 25°C), which generally increases with rising P-T due to higher degrees of self-dissociation (Holzapfel, 1969). However, pure water does not exist in nature given its potency as a solvent. Freshwater has enough ions in solution that its EC is enhanced by two to four orders of magnitude. Indeed, EC is so sensitive to the total concentration of ions in dilute solutions that it is routinely used to test for mineral content and drinking water quality (e.g., Sappa et al., 2014).

For crustal scale EM studies involving aqueous fluids in porous media, the EC of the fluid is typically estimated from experimental data on sodium chloride (NaCl) solutions as that is the most abundant salt present in the water and the mobility of other common ionic species is of similar magnitude (Nesbitt, 1993). For example, mean seawater has about 3.5 wt% dissolved salts, of which 1.9 wt% is Cl^- and 1.1 wt% is Na^+ ions.

Recent advancements have significantly increased the range of P-T conditions under which EC measurements on saline fluids are possible, from 0.4 GPa and 800°C (e.g., Quist & Marshall, 1968) to 5 GPa and 900°C (Guo & Keppler, 2019). Sinmyo & Keppler (2017) developed the following equation to fit their data with a linear regression

$$\log \sigma_f = A_1 + A_2/T + A_3 \log c + A_4 \log \varrho + \log \Lambda_0 \tag{14}$$

$$\Lambda_0 = \lambda_1 + \lambda_2 + \lambda_3/T + \lambda_4/T^2 \tag{15}$$

where A_i are constants, T is the absolute temperature, c is the NaCl concentration in wt%, ϱ is the density of pure water in g/cm³ (at given P-T), Λ_0 is the molar conductivity at infinite dilution in S·cm²/mol (at given P-T), and λ_i are constants. Although small fractions of highly saline fluids can readily explain most EC observations, the chemical and mechanical stability of pore fluids at depth is debated (e.g., Yardley & Valley, 1997; 2000; Wannamaker, 2000)

and must be considered if they are to be invoked as a cause for conductive anomalies, which is beyond the scope of this review.

2.2.2 Molten silicates and carbonates

As is the case for aqueous solutions, the EC of molten minerals is also governed by the concentration and mobility of the various ionic species but where the bulk chemistry plays a critical role (e.g., composition, amount of alkali, degree of polymerization, concentration of volatiles dissolved in the melt). Here we briefly describe the EC dependence of carbonated hydrous silicate melt, specifically mafic (basaltic) melts as they are most relevant to the asthenosphere. We refer the reader to previous reviews of melt conductivity for more insight on the electrical behavior of other silicate melts (e.g., Pommier, 2014; Ni et al., 2015; Yoshino, 2018).

Anhydrous basaltic melts are several orders of magnitude more conductive than their source rock (Rai & Manghnani, 1977; Tyburczy & Waff, 1983). The addition of water further enhances the EC by around one order of magnitude (Ni et al., 2011). Yet hydrous basaltic melts are still two to three orders of magnitude less conductive than carbonatite melts (Yoshino et al., 2010; Sifré et al., 2014). The significant effect of both H_2O and CO_2 on the conductivity of carbonated hydrous basaltic melts is expressed in the semi-empirical relationship of Sifré et al. (2014)

$$\sigma_{\text{melt}} = \sigma_{H_2O} + \sigma_{CO_2} = \sigma_{0,H_2O} \exp\left(-\frac{\Delta E_{H_2O}}{RT}\right) + \sigma_{0,CO_2} \exp\left(-\frac{\Delta E_{CO_2}}{RT}\right) \quad (16)$$

where the activation energy and pre-exponential factor of each volatile species (H_2O and CO_2) depends on its concentration

$$\Delta E_{\text{volatile}} = a \exp(-bC_{\text{volatile}}) + c \quad (17)$$

$$\ln \sigma_{0,\text{volatile}} = d\Delta E_{\text{volatile}} + e \quad (18)$$

where a, b, c, d, and e are constants and C_{volatile} is the H_2O or CO_2 content in wt%.

2.3 Conduction in multi-phase media

Our capability to model the physical properties (such as EC) of the Earth's crust and mantle directly depends on our understanding of its mineralogy, thermal state, and pore fluid content. At a defined temperature, the bulk EC of a multi-phase assemblage strongly depends on the geometry and interconnectivity of each phase, especially when one is much more conductive than the other(s). Several formalisms, such as the commonly used Archie's law and Hashin-Shtrikman (HS) bounds, have been proposed and reviewed in detail elsewhere (e.g., Glover et al., 2000; ten Grotenhuis et al., 2005; Glover, 2010; Miller et al., 2015).

An isolated phase present in a small amount is unlikely to contribute significantly to the bulk EC, even if its intrinsic conductivity is high. In order to be detected by EM methods such as MT, a high-conductivity phase needs to be interconnected over some finite region that is

large enough to influence the data. This configuration is expected in geological contexts where fluids are present, such as at volcanic areas (e.g., Müller & Haak, 2004; Aizawa et al., 2014; Pommier et al., 2010; Bedrosian et al., 2018), mantle upwelling zones (e.g., Wannamaker et al., 2008; Comeau et al., 2018), mid-ocean ridges (e.g., Caricchi et al., 2011; Key et al., 2013; Johansen et al., 2019), and subduction zones (e.g., Worzewski et al., 2011; McGary et al., 2014; Laumonier et al., 2015; Heise et al., 2017).

2.3.1 Multi-phase porous media

The simplest mixtures consist of two phases: a porous solid saturated in fluid. The routinely used Hashin-Shtrikman formulation provides theoretical bounds on the EC of homogeneous isotropic mixtures (Hashin & Shtrikman, 1962). It assumes a volume packed with spheres where the outer shell of each sphere is made up of one phase and the core of the other phase. For the upper bound (HS^+), the outer shell is the conductive phase and the core is the resistive phase, and vice versa for the lower bound (HS^-)

$$\sigma_{\text{bulk}}^{HS^+} = \sigma_c \left[1 - \frac{3\phi_r(\sigma_c - \sigma_r)}{3\sigma_c - \phi_c(\sigma_c - \sigma_r)}\right] \tag{19}$$

$$\sigma_{\text{bulk}}^{HS^-} = \sigma_r \left[1 + \frac{3\phi_c(\sigma_c - \sigma_r)}{3\sigma_r + \phi_r(\sigma_c - \sigma_r)}\right] \tag{20}$$

where σ_c and ϕ_c are the EC value and the volume fraction of the conductive phase and σ_r and ϕ_r are the EC value and volume fraction of the resistive phase, respectively.

In cases where the fluid is several orders of magnitude more conductive than the host rock, the fluid conductivity and the porosity can be used to estimate the bulk EC. One such widely applied empirical relationship is Archie's law (Archie, 1942)

$$\sigma_{\text{bulk}} = \sigma_f \phi^m \tag{21}$$

where σ_f is the fluid conductivity, ϕ is the porosity (volume fraction), and m is the empirically derived Archie's exponent. In practice, the observed quantity is the bulk EC and the desired quantity is either the porosity or pore fluid conductivity. Archie's law was developed specifically for porous media with relatively uniform pore geometries such as unconsolidated sediments and sedimentary rocks. It has also been successfully applied to fractured crustal rocks (e.g., Brace & Orange, 1968; Becker, 1985; Key et al., 2012) and partially molten rocks (e.g., Miller et al., 2015). A significant advantage of Archie's law is the flexibility afforded by the exponent variable m. A commonly used value is $m = 2$, with most applications adopting values between 1.5–2.5 and slightly higher in carbonates (Glover, 2010). However, Archie's law cannot be applied universally in its original form. Numerous variants have been proposed for specialized cases, such as for clay-bearing mixtures where a unique surface conduction process operates (e.g., Waxman & Smits, 1968).

There are also mixing models for more than two phases. The geometric mean is commonly used for randomly distributed mixtures

$$\sigma_{\text{bulk}} = \prod_i \sigma_i^{\phi_i} \tag{22}$$

where σ_i is the EC of the ith phase and exponent ϕ_i is the volume fraction of the ith phase. Alternatively, Archie's law has been generalized to accommodate any number of phases and geometrical constraints on the distribution (Glover, 2010)

$$\sigma_{\text{bulk}} = \sum_i \sigma_i \phi_i^{m_i} \tag{23}$$

$$m_j = \frac{\log\left(1 - \sum_{i \neq j} \phi_i^{m_i}\right)}{\log\left(1 - \sum_{i \neq j} \phi_i\right)} \tag{24}$$

As is the case for the conventional form of Archie's law in Eq. 21, the Archie's exponent is a variable that provides valuable flexibility for tailoring to specific applications. However, since the m values for systems with three or more conducting phases such as mantle rocks have relatively few constraints, this flexibility is also a source of uncertainty.

2.3.2 Multi-phase mantle

When the difference in EC values is small or moderate for all phases that make up the aggregate, it is tempting to simplify the system by assuming that, to first approximation, the bulk EC corresponds to the conductivity of the most abundant phase. However, this simplification may lead to a significant bias in physical property estimates that can be deduced from electrical measurements. For instance, EC models of the Earth's upper mantle often assume an olivine-only mineralogy, olivine being both the most abundant mineral in this part of the mantle and the most widely measured in conductivity experiments. Recent studies demonstrate this simplification of mantle chemistry has significant effects on the interpretation of bulk mantle EC observations and that accurate estimations require incorporating a more realistic petrology (e.g., Fullea et al., 2011; Khan, 2016; Naif, 2018; Selway et al., 2019; Özaydin & Selway, 2020). Below we provide a working example of how composition affects mantle temperature.

Xenoliths have shown that olivine, pyroxene, and garnet are all present in significant amounts in the upper mantle (e.g., Stachel et al., 2005). Let us consider a typical peridotite composition for the convecting asthenosphere with 55 vol% olivine, 25 vol% pyroxene, and 20 vol% garnet. Using the EC studies for each phase, we computed the bulk EC of the corresponding bulk mantle over 900–1400°C. For each temperature, calculations were performed using Eq. 22 for the geometric mean (e.g., Shankland & Duba, 1990). However, if we consider a rock with isolated garnet grains (i.e., not interconnected; Boullier & Nicolas, 1975), using the geometric mean overestimates the influence of garnet on the bulk EC. This is evident when applying the generalized Archie's law in Eq. 23 to more "realistically" predict the bulk EC. Taking the Archie's exponent of pyroxene and garnet to be 1.3 and 5, Eq. 24 requires m~0.3 for olivine. The results are presented in Figure 3.

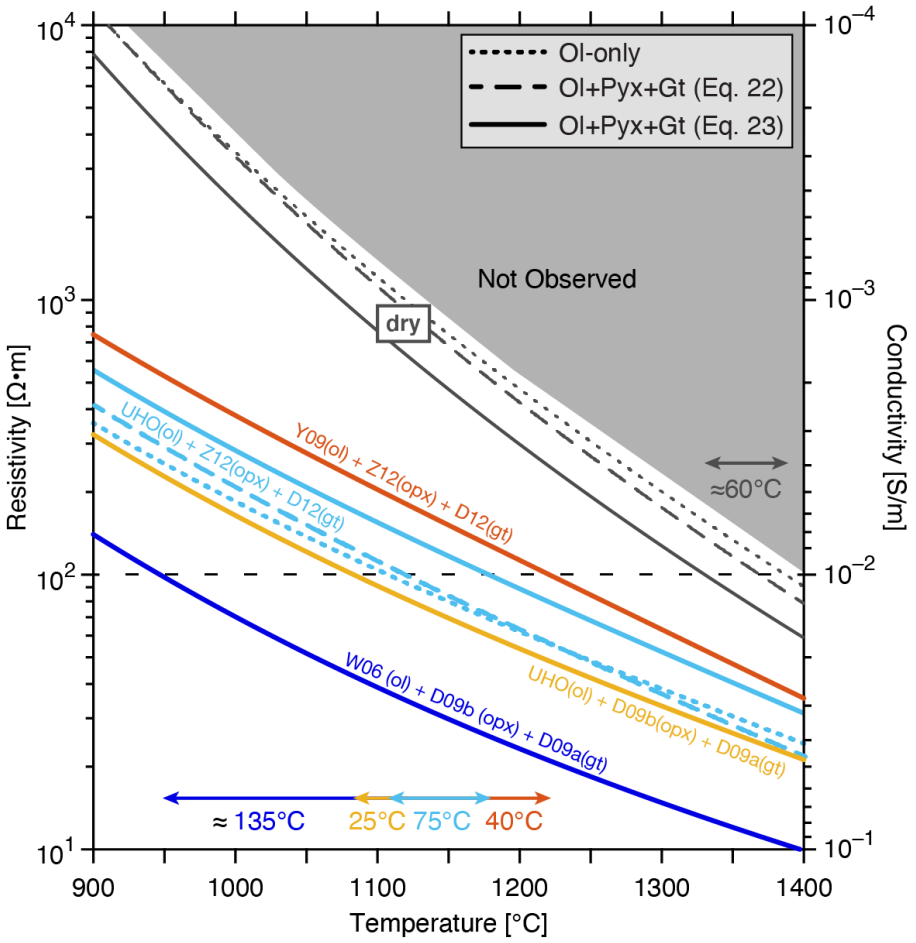

Figure 3: *Effect of mantle chemistry, water distribution, and geometric mixing models on electrical conductivity. Grey lines are for dry mantle and colored lines for 200 ppm water. Dotted lines assume an olivine-only composition, while dashed and solid correspond to a mixture of 55 vol% olivine, 25 vol% pyroxene, and 20 vol% garnet. Water partition coefficient for pyroxene/olivine (D=10) and garnet/olivine (D=2) are from Hauri et al. (2006). Model curves calculated with Eq. 22 (dashed lines) use the geometric mean mixing model, while those using Eq. 23 (solid lines) use the generalized Archie's law formulation with Archie's exponent values of 1.3 and 5 for pyroxene and garnet. Colored arrows indicate the temperature uncertainties that result from considering different EC models and geometric mixing models. The grey area represents the "forbidden zone" of physically unrealizable resistivity-temperature combinations. See text for details.*

For an anhydrous ("dry") mixture, the EC difference between an olivine-only mantle and the geometric mean of a three-phase mantle is moderate, equivalent to about 60°C uncertainty for 100 Ω·m mantle (Fig 3). This is because dry garnet is approximately half an order of magnitude more conductive than orthopyroxene and one order of magnitude more conductive than olivine (Dai & Karato, 2009a; Dai et al., 2012; note that other laboratory studies found garnet to be only slightly more conductive than olivine, e.g., Romano et al., 2006). By comparison, the difference is small for the generalized Archie's law calculation

since it downweighs the influence of garnet. This makes it tempting to justify the application of an olivine-only mineralogy when estimating the EC of dry mantle. However, the Archie's exponents are not fixed quantities and are often poorly known (e.g., Glover et al., 2000; Laumonier et al., 2017). Therefore, given the increasing availability of EC values for different minerals and the relative simplicity of generating multi-phase models, we suggest always comparing the olivine-only dry mantle conductivity with more realistic mixtures to justify using the former.

For a wet mantle, moderate to large EC differences are predicted depending on the mineralogy (olivine-only or mixture of minerals), the water distribution between the different minerals, and the choice of EC models. Let us consider the UHO (olivine), Z12 (orthopyroxene), and D12 (garnet) conductivity models as well as a bulk mantle water content of 200 ppm, which is consistent with estimates for mid-ocean ridge basalt (MORB) source in the upper mantle (50–250 ppm) from previous studies (e.g., Saal et al., 2002; Hirschmann, 2006). When accounting for water partitioning values (using partition coefficients $D_{\mathrm{pyx/ol}} = 10$ and $D_{\mathrm{gt/ol}} = 2$; from Hauri et al., 2006), the olivine, garnet, and pyroxene have about 58, 116, and 580 ppm water, respectively. In this example, the choice of mixing model has a moderate effect on the mantle temperature estimate (~75°C). At a bulk resistivity value of 100 Ω·m, an olivine-only mantle with 200 ppm water (dotted cyan line) yields a temperature estimate of about 1107°C, whereas accounting for composition and water partitioning yields 1123°C for a geometric mean mixture (Eq. 22; dashed cyan line) or 1180°C for a generalized Archie's law mixture (Eq. 23; solid cyan line), i.e., 16°C or 73°C higher than for a simplistic mantle chemistry. Note that the hydrous mantle mixtures can be more resistive than the olivine-only resistivity because the olivine phase in the former has only 58 ppm water compared with 200 ppm in the latter.

The uncertainty has a greater dependence on which EC models are applied than it does on the choice of mixing model. For instance, replacing the UHO model with Y09 for olivine gives the most resistive prediction, increasing the temperature estimate to 1220°C. If instead we replace the UHO, D12, and Z12 models with the most conductive models for olivine (W06), garnet (D09a), and pyroxene (D09b), the temperature estimate decreases to 947°C. These simple calculations highlight the importance of combining geochemical constraints and petrological knowledge with competing EC measurements when interpreting EM observations.

It should be noted that the formalisms mentioned above do not account explicitly for the contribution of grain boundaries to the bulk EC, though grain boundaries can be considered as an independent phase with a specific conductivity value (e.g., Roberts & Tyburczy, 1993). Their contribution can be significant, especially in natural rocks with fine-grain size where impurities are present between grains. Grain boundaries represent fast diffusion pathways in polycrystalline materials, and diffusivities can be orders of magnitude faster than through

grains (e.g., Dohmen & Milke, 2010). The flux of impurities through a polycrystalline aggregate, and the resulting conductivity, depends on the mobility of the diffusing species and on its concentration along the fastest pathway (i.e., grain boundaries). Grain boundaries are fast pathways for both ionic (e.g., Watson, 2002) and electronic species (e.g., Roberts & Tyburczy, 1991). In fine-grained olivine aggregates, electronic conduction usually dominates ionic conduction along grain boundaries, due to a much higher concentration of electronic charge carriers in grain boundaries relative to ionic species (with the possible exception of protons) (Pommier et al., 2018).

2.4 The effect of rock deformation on electrical conductivity

The motion of rigid lithospheric plates relative to the underlying convecting mantle results in the deformation of the asthenosphere. Both experimental and computational investigations have demonstrated that deformed polycrystalline materials develop strong microtextures, characterized by crystallographic preferred orientations of the grains and a preferential distribution of the grain boundaries (e.g., Ghosh & Karki, 2014; Hansen et al., 2014; Marquardt et al., 2015). The resulting microstructure affects the bulk electrical properties of deformed materials, and in particular, causes electrical anisotropy.

The few studies performed on melt-bearing sheared samples (Caricchi et al., 2011; Zhang et al., 2014; Pommier et al., 2015) observed electrical anisotropy attributed to the preferential connectivity of the melt phase in the direction parallel to the main shear direction. In dry, melt-free olivine aggregates with shear strains up to ~7.3 and grain sizes <~15 μm, it has been demonstrated that grain boundaries become the dominant conduction path and that grain boundary conduction is electrically anisotropic, as much as a factor of four more conductive in the shear direction than normal to the shear plane (Pommier et al., 2018). This suggests that the interpretation of EM data in lithospheric shear zones (where grain sizes are extremely small) requires considering the effect of rock deformation on the bulk EC in addition to the influence of water and/or melt. For coarser grain-size materials, it is likely that the EC would be dominated by the intragranular flux of electronic defects (e.g., Roberts & Tyburczy, 1993).

2.5 Electrical conductivity and viscosity

One grand challenge that is a nascent area of research for mantle applications is to use electrical conductivity as a proxy for viscosity since water content, temperature, and partial melt content are also primary controls on mantle viscosity (e.g., Hirth & Kohlstedt, 2003). Viscosity is critical for understanding the dynamics of fundamental geologic processes, such as the efficient focusing of mantle melts generated over a wide region as they ascend and erupt in a narrow zone at mid-ocean ridges and volcanic arcs (e.g., Wilson et al., 2014; Sim et al., this issue). A few studies have attempted to estimate melt and mantle viscosity empirically from electrical conductivity (e.g., Pommier et al., 2013; Selway, 2015; Liu & Hasterok, 2016; Xu et al., 2018; Selway et al., 2020).

In basaltic melts, water dissolution significantly decreases viscosity (Persikov et al., 2017) and increases conductivity (Ni et al., 2011), suggesting a correlation between both transport properties, as previously demonstrated experimentally in other dry silicate melts (Grandjean et al., 2007). The effect of hydrogen (and possibly other volatiles) on the viscosity and conductivity of silicate melts strongly depends on temperature, species oxidation state, and melt polymerization. A better understanding of these transport properties is required to understand the magmatic processes that govern present-day mantle dynamics.

3. Introduction of MT method

The primary geophysical tool used to image EC of the lithosphere-asthenosphere system is magnetotelluric (MT) method. Here we provide a brief overview of basic concepts. Vozoff (1991) is a classic reference on the MT method, and many additional details can be found in Chave & Jones (2012). The fundamental physical basis for all EM methods is Faraday's law: a time-varying magnetic flux induces an electric field, which can drive currents in a conductor. The MT method is a passive-source geophysical method, relying on natural time variations in magnetic fields impinging on Earth's surface that induce electric currents in the subsurface. At frequencies above 1 Hz, the source fields arise mostly from radiation (in the electrically insulating atmosphere) of EM fields due to lightning. At the lower frequencies that are most relevant to the deeper Earth considered here, sources of magnetic variations lie in the ionosphere and magnetosphere, driven primarily by interactions of Earth's main field with the solar wind, and convection/neutral winds in the conducting ionosphere.

The raw data for the MT method are magnetic and electric field time-series. Magnetic field vectors (usually including vertical components) are measured with induction coil or fluxgate magnetometers (e.g., Constable, 2013). Electric fields (two horizontal components) are derived from measurements of electric potential between pairs of buried non-polarizing electrodes, typically separated by ~100 m (the larger the separation the higher the signal-to-noise ratio). Raw data are transformed to the frequency domain via Fourier transform of a series of short overlapping time windows, and the resulting sequence of Fourier coefficients are used to estimate an impedance tensor $\boldsymbol{Z}(f)$ defining a frequency-dependent linear relationship (or transfer function) between horizontal magnetic ($\boldsymbol{H}$) and electric ($\boldsymbol{E}$) components

$$\boldsymbol{E} = \boldsymbol{Z}(f)\boldsymbol{H} \tag{25}$$

Transfer functions (TFs) that relate the vertical and horizontal magnetic field components (often referred to as "Tippers") are also commonly estimated and used in resistivity imaging. In either case, the statistical TF estimation problem is generally solved with robust methods (e.g., Egbert & Booker, 1986), since field data are all too often contaminated with sporadic bursts of noise (e.g., from anthropogenic EM sources). Most often, magnetic data from a simultaneously occupied second site are used as a "remote reference" for noise cancellation

(Gamble et al., 1979). Modern methods for TF estimation are summarized in Egbert (2011) and more extensively reviewed in Chave (2012).

Maxwell's equations in the quasi-static limit describe the physics of EM induction. In this low-frequency limit, where displacement currents can be neglected in comparison to conduction currents, propagation of EM fields in a conductor is described by a diffusion equation. In the simplest case of a uniform or layered one dimensional (1D) Earth, the equations are identical to those used to describe heat conduction. Thus, variations imposed at the surface (as assumed for MT, where sources are external to the Earth) decay exponentially with depth

$$\delta = \sqrt{\frac{\rho T}{\pi \mu_0}} \approx 500\sqrt{\rho T} \tag{26}$$

where δ is the skin depth in meters, ρ is the resistivity in Ω·m, T is the period in seconds, and μ_0 is the magnetic permeability of free space (equal to $4\pi \times 10^{-7}$ H/m). At one skin depth, the field amplitudes at the surface decay to $1/e$ (e being the natural logarithm), or about 37%. The dependence of skin depth on period means that lower-frequency signals penetrate more deeply and will be sensitive to deeper structure. As simple examples, the skin depths of a 10 Ω·m half-space at 10, 100, and 1000 s periods are approximately 5, 16, and 50 km, respectively. Skin depths at the same periods would be reduced for a less resistive (more conductive) Earth.

Controlled-source electromagnetic (CSEM) methods are also used for imaging subsurface EC, often with higher resolution than MT data, but for practical transmitter powers the depth of investigation is limited to the uppermost crust. The marine CSEM method is an exception. In the ocean, the skin depth of seawater is less than 1 km at 10 s period. Therefore, the high-frequency EM fields are significantly attenuated, which limits the marine MT data to periods longer than about 20 s in most ocean basins (e.g., Key & Constable, 2002). As a result, marine MT data have limited resolution to the EC structure in the top 10 km or so (depending on the thickness of conductive sediments). However, the high conductivity of seawater allows much larger transmitter power outputs, typically at periods of 0.1-10 s, and makes marine CSEM suitable for imaging EC structure in the crust and uppermost mantle where the marine MT data lack sensitivity (e.g., Cox et al., 1986; Constable, 2013).

The skin depth provides a length scale that is critical to the MT method in another way. Provided that the length scale L that the external source varies over satisfies $L \gg \delta$, the impedance is independent of details of the source, which can then be assumed to be spatially uniform. Indeed, this uniform source assumption is central to the MT method, allowing measurements in a point (which of course could not constrain external source geometry) to be used for EM sounding. Because source length scales are typically thousands of km this assumption is generally well justified, although this may not be true close to the magnetic

poles (e.g., Peacock & Selway, 2016) or in the presence of geomagnetic pulsations (Murphy & Egbert 2018). In the 1D case where resistivity varies only with depth, the impedance tensor reduces to

$$\boldsymbol{Z} = \begin{bmatrix} 0 & Z \\ -Z & 0 \end{bmatrix} \tag{27}$$

The scalar impedance is then just the ratio of orthogonal electric and magnetic field components at the appropriate frequency f. For a uniform Earth of resistivity ρ, the magnitude of the impedance takes the simple form $|Z| = \sqrt{2\pi\mu_0\rho/T}$. This justifies the definition of an apparent resistivity (ρ_a) for the MT method—i.e., for any impedance, ρ_a is the resistivity of a uniform Earth that would explain the observed impedance amplitude

$$\rho_a = \frac{T}{2\pi\mu_0}|Z|^2 \tag{28}$$

Since magnetic and electric fields are complex numbers in the frequency domain, the impedance also has a phase, with the electric field component (e.g., E_x) generally leading the corresponding orthogonal magnetic component (H_y). In a uniform Earth (no variation of resistivity with depth), the phase lead is 45 degrees. When resistivity is decreasing with depth, phases are elevated; when resistivity is increasing with depth, phases drop below 45 degrees (see MT response figures in Section 4). Apparent resistivity and phase are related through the Hilbert transform for a 1D Earth.

If Earth resistivity is two dimensional (2D), with no variation along a preferred strike (for example, along a fault separating distinct crustal blocks), the impedance tensor also takes a simplified form

$$\boldsymbol{Z} = \begin{bmatrix} 0 & Z_{xy} \\ Z_{yx} & 0 \end{bmatrix} \tag{29}$$

provided the coordinate system aligns with geologic strike, which we take to be in the direction of the *x*-axis. In this case, the MT response decouples into TE (transverse electric) and TM (transverse magnetic) modes, corresponding to Z_{xy} and Z_{yx}, respectively. Electric currents flow along the geologic strike for the TE mode, while for the TM mode current flows across strike. In the general case where resistivity variations are three dimensional (3D), all four components of the impedance will be nonzero. However, in almost all cases, the off-diagonal components of the impedance tensor dominate (as in the 1D and 2D cases) and so the common practice is to focus more on these in MT interpretation.

Since the measured data vary with subsurface dimensionality, it is possible to analyze MT data to determine the dimensionality of the Earth, calculate a geoelectric strike direction (if present) and determine an appropriate inversion approach. There is an essentially complete theory for 1D inversion of MT response curves (apparent resistivity and phase as a function of frequency) at a single site for EC-depth profile (Whittall & Oldenberg, 1992). While this

1D approach is still used to get a quick estimate of subsurface EC profiles beneath each site (e.g., Hamilton et al., 2006), in most modern applications impedance components from multiple sites are inverted for 2D or 3D EC using standard regularized inversion methods, i.e., a functional that penalizes data misfit and some measure of model roughness is minimized. Because the forward problem (mapping EC to impedances) is nonlinear, gradient-based schemes (e.g., Gauss-Newton, conjugate gradients, quasi-Newton) are generally used. These still require the partial differential equations of EM induction (the quasi-static Maxwell equations in a conductor) to be solved thousands of times, so (especially in 3D) the inverse problem is computationally intensive. A survey of methods used for MT inversion can be found in Rodi & Mackie (2012). Examples of widely used 2D inversion codes include Occam2D (de Groot-Hedlin & Constable, 1990), and MARE2DEM (Key, 2016), while some commonly used 3D inversion codes include WSINV3DMT (Siripunvaraporn et al., 2005) and ModEM (Egbert & Kelbert, 2012; Kelbert et al., 2014).

As in all geophysical inverse problems, an infinite number of EC models can adequately fit the field data. Different regularizations or parameterizations will produce different results, so any single inverse model is inherently subjective (Constable et al., 2015), and models presented in the literature are thus often referred to as the "preferred model." Many strategies attempt to address this intrinsic non-uniqueness and to understand what features are resolved and required by the data. One widely used approach is to test robustness of a particular feature in the preferred inverse solution (say a conductive anomaly of interest) by altering its conductivity, forward calculating the MT responses, and comparing the model-to-data misfit against the original inversion. If the misfit is not increased significantly, the feature is obviously not required by the data. An extension of this idea is "hypothesis testing," where model features are added or removed, and the inversion is restarted with the resistivity of the modified feature "frozen" to the specified value. Note that the sort of checkerboard tests commonly used in seismic tomography are not often useful for MT data, due to the significantly greater nonlinearity of the inverse problem (Burd et al. 2014). Bayesian approaches to quantifying model uncertainty are also being pursued, but the computational burden is significant enough that this is so far only tractable for 1D applications (e.g., Blatter et al., 2019).

4. EC predictions of lithosphere-asthenosphere system

For the remainder of this review, we focus on the 1D forward problem. We generate a suite of depth-dependent EC predictions for different physical states and then forward model the MT responses. This allows us to probe questions such as (i) how distinct the EC predictions are for a variety of expected mantle states and what the potential sources of ambiguity are; and (ii) how sensitive the MT data are to changes in temperature, composition, and the other physical properties of interest. Even in our final example, a case study of the lithosphere beneath the southeastern United States, where fully 3D inversion was used to interpret an

array of several hundred MT sites, considerable insight can be obtained from this 1D analysis.

4.1 Oceanic Mantle

The oceanic lithosphere-asthenosphere system is far simpler than its continental sibling. Away from the influence of hotspots and plate boundaries, ocean basins have a relatively uniform layered structure with small deviations from the global mean: a veneer of pelagic sediment, a 6–7 km thick mafic crust, and a peridotite upper mantle.

Our oceanic resistivity models consist of five compositionally distinct layers: atmosphere, seawater, marine sediment, mafic crust, and peridotite upper mantle. The lower atmosphere is an excellent insulator and typically exceeds 10^{12} Ω·m (Singh et al., 2004). In contrast, the deep ocean is highly conductive with an average value of 0.3 ± 0.03 Ω·m, which has tight bounds since seawater salinity varies by less than 10% from the global mean and the temperature in waters deeper than 1 km is within a few degrees of 3°C. We treat the sedimentary and crustal units as porous media containing a conductive fluid (seawater) in a resistive matrix and apply Archie's law (Eq. 21). For convenience, we ignore clay content and assign the Archie's exponent value $m = 2$. Due to the geothermal gradient, we calculate the seawater EC as a function of mean layer temperature with the cubic relationship of Constable et al. (2009). The sediment layer is 0.5 km thick and 0.8 Ω·m (60% porosity, 5°C). The oceanic crust consists of three sublayers with distinct porosities: extrusive basalts, sheeted dikes, and gabbros. We adopt realistic porosities and thicknesses for the crustal layers based on a global compilation of these properties by Jarrard (2003). The extrusive layer is 500 m thick and 20 Ω·m (10% porosity, 20°C). The dike layer is 1.5 km thick and 150 Ω·m (3% porosity, 45°C). The gabbro layer is 4.5 km thick and 1250 Ω·m (0.7% porosity, 120°C). These estimates are also consistent with marine CSEM observations of the oceanic crust (Key et al., 2012; Naif et al., 2015; Chesley et al., 2019). Since the characteristic porosity and thickness of oceanic crust does not deviate much from the global mean (e.g., White et al., 1992; Jarrard, 2003), we use the same crustal resistivity trend in all of our oceanic models.

4.1.1 Anhydrous mantle

Our first set of models aims to isolate the electrical effect of temperature by considering dry upper mantle of fixed peridotitic composition. We adopt the compositional model of Hirschmann et al. (2009), which contains 60 vol% olivine (this includes 2 vol% spinel that we handle as olivine) and depth-dependent proportions of orthopyroxene, clinopyroxene, and garnet (Fig 4a). Next, we calculate the depth-dependent temperature profiles with the Hasterok (2013) plate cooling model for six plate ages (5, 10, 20, 40, 80, and 160 Ma) at two mantle potential temperatures (MPTs) (1350°C and 1420°C). A 0.3°C/km adiabatic gradient is added. The 12 geotherms are shown in Fig 4b. We use the temperatures to estimate the EC for dry olivine (Constable, 2006), dry orthopyroxene (Zhang et al., 2012), dry clinopyroxene

(Zhao & Yoshino, 2016), and dry garnet (Dai & Karato, 2009a). Then, we apply the geometric mean (Eq. 22) to get the bulk mantle EC shown in Fig 4c.

The forward-modelled MT responses and the relative differences between them are presented in Fig 5 to showcase the data dependence on mantle temperature. Interestingly, although the EC predictions differ for the two oldest ages, their respective MT responses are identical. Even the 40 Ma responses do not differ appreciably from those of 80/160 Ma, which suggests a lack of data sensitivity to highly resistive mantle. To test for the maximum resistivity to which the MT data are sensitive, we take the EC prediction for the 160 Ma plate (1350°C MPT) and impose an upper bound on the mantle resistivity, progressively lowering it until the forward modelled MT responses are impacted. The responses changed by up to 1.5% and 7.5% when the upper bound was reduced to 5000 Ω·m and 1000 Ω·m, respectively. MT data errors vary from survey to survey but in practice are on the order of 2–10%. Therefore, given that 5000 Ω·m dry peridotite mantle corresponds to about 1070°C, MT data are insensitive to colder temperatures since they cannot distinguish higher resistivities. Note, however, that the greater the thickness of a highly resistive lithosphere, the more sensitive the MT data are to its true resistivity value. For example, when we consider a 150 km thick resistive lithosphere, twice the thickness as the previous test, the responses changed by up to 3% and 13.5% when the upper bound was reduced to 5000 Ω·m and 1000 Ω·m, respectively.

The lack of sensitivity to highly resistive features is expected when we consider that the MT method is better at constraining the conductance (the product of conductivity and thickness, units of siemens [S]) than at resolving resistivity with depth. For example, in our oceanic models the sediment layer, which is 0.5 km thick and 0.8 Ω·m (1.25 S/m), has a conductance of 625 S, whereas the top 50 km of upper mantle is just 0.2 S for the 80 Ma plate and 0.1 S for the 160 Ma plate. Therefore, the presence of the conductive sediment layer alone significantly hinders the ability of the data to resolve resistive features. This would then imply that either reducing the thickness or increasing the resistivity of the sediment layer in our models would significantly increase sensitivity to the highly resistive portion of the lithosphere, which is indeed the case. For the 160 Ma plate model now with a sediment layer resistivity of 4 Ω·m (equivalent to 125 S), applying a 5000 Ω·m upper bound on mantle resistivity impacts the responses by almost 6%, compared to 1.5% in the original model with 0.8 Ω·m sediment. In addition to the conductance, the skin depth approximation (Eq. 26) also provides valuable insight. Specifically, even if we remove the sediment layer from the models altogether, the MT data would still underestimate the resistivity of the cold shallow lithosphere simply due to the deeper presence of a warm and therefore conductive asthenosphere. Regardless, even if the MT data were able to resolve 10^5 Ω·m mantle, this would only correspond to about 850°C. We note that in contrast to the MT method, CSEM data are highly sensitive to resistors and can resolve both the resistivity value and anisotropy of the lithosphere (e.g., Chesley et al., 2019).

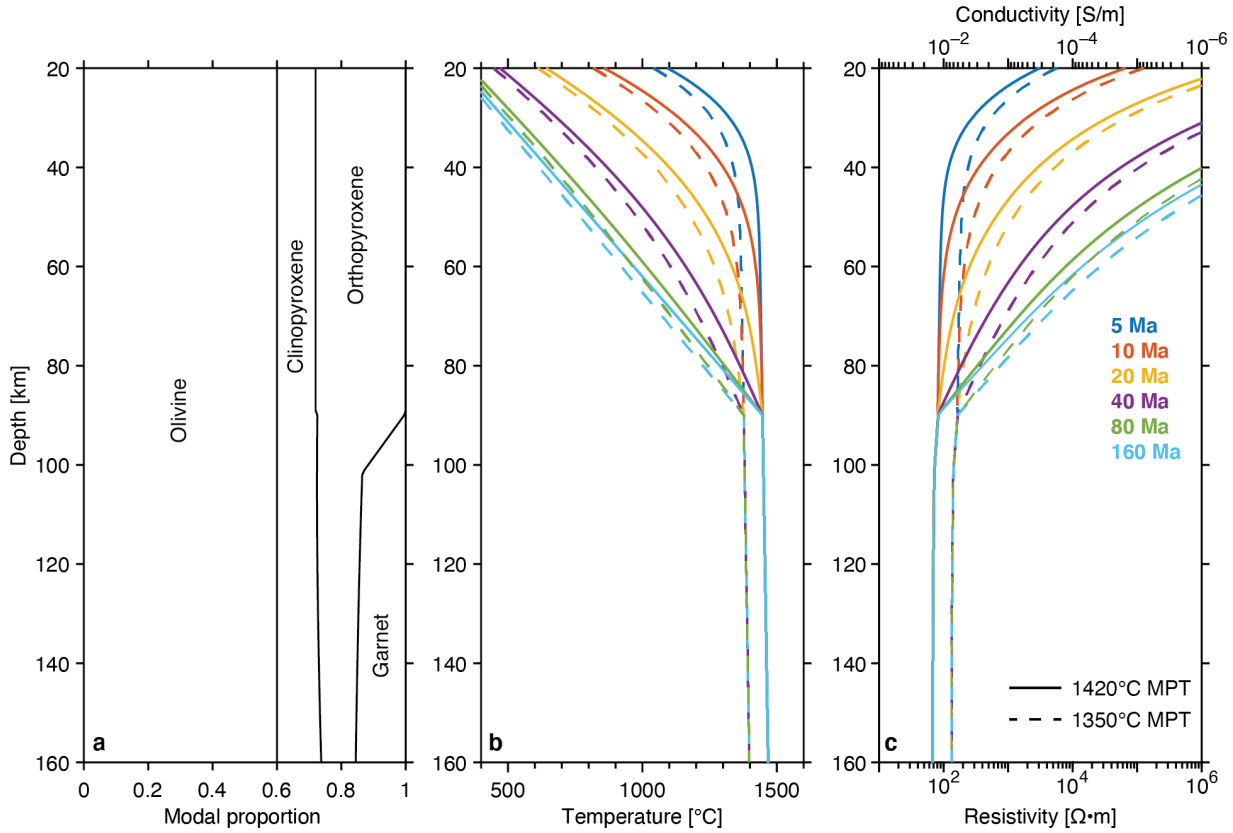

Figure 4: *(**a**) Oceanic upper mantle peridotite composition. (**b**) Plate geotherms for 5, 10, 20, 40, 80, and 160 Ma lithosphere from Hasterok (2013) plate cooling model. Solid lines use 1420°C MPT and dashed lines use 1350°C MPT. (**c**) Predicted bulk mantle EC/resistivity for the composition in panel (**a**) and all 12 geotherms in panel (**b**). Depth is in kilometers below seafloor.*

All of the apparent resistivity (AR) curves in Fig 5 are remarkably similar at less than 100 s period regardless of the MPT, with only small differences in phase that are equivalent to <5% error (10% error in phase is ±2.85 degrees). This is because the MT responses are mostly sensing the same sediment, crust, and highly resistive structure in the uppermost mantle that the data cannot distinguish. As the data sense the deeper more conductive mantle with longer periods, the AR curves for the different plate ages diverge and become distinguishable, with peak separation at around 500–1000 s. This also happens to be where the phase curves in each set of MPT models crossover, indicating the data are sensitive to a change in the resistivity gradient with depth. Phase curves can be thought of as reflecting the resistivity gradient, where phases <45° signify increasing resistivity with depth, phases >45° signify decreasing resistivity with depth, and phases of 45° signify homogeneity (see Ch 2.5 in Simpson & Bahr, 2005). At periods longer than 1000 s, the AR curves within each set of MPT models begin to converge as the data become increasingly sensitive to the asthenosphere, where the EC is no longer dependent on plate age but only depth. At periods of about 5000 s, the phase exceeds 45°, indicating sensitivity primarily to the conductive asthenosphere and deeper mantle. Taken together, this set of models suggests that, in the

dry mantle case, the MT data provide constraints on temperatures in excess of ~1000°C, keeping in mind that field data typically have errors of ~5%.

4.1.2 Hydrous mantle

Although NAMs are significantly more conductive under hydrous conditions, predicting the bulk mantle conductivity depends strongly on a set of underlying assumptions that are either debated or poorly constrained. The two leading uncertainties are choice of empirical EC law for a given mineral (see Fig 2) and choice of mixing model (see Fig 3). We will only consider the former here.

Since garnet is less abundant than olivine and pyroxene and there are currently no competing EC models for hydrous clinopyroxene, we follow the approach of Naif (2018) and simplify the composition to just olivine and orthopyroxene. First, we adopt the suite of partition coefficients defined in Hirschmann et al. (2009) but replace the pyroxene coefficients with updated values from O'Leary et al. (2010). We use these coefficients to determine the water concentration in each mineral (olivine, garnet, orthopyroxene, clinopyroxene) for 200 ppm water in the bulk mantle. We also account for the extraction of water by partial melting during oceanic lithosphere formation at the ridge axis, which renders the mantle dry at the shallower depths (<70 km) where dry melting occurs (e.g., Hirth & Kohlstedt, 1996; Dasgupta et al., 2007). The resulting water distribution is presented in Fig 6a.

Next, we simplify the composition by combining the garnet with olivine while also preserving the bulk mantle water content

$$C_{\mathrm{o/g}} = \frac{\phi_{\mathrm{ol}} C_{\mathrm{ol}} + \phi_{\mathrm{gt}} C_{\mathrm{gt}}}{\phi_{\mathrm{ol}} + \phi_{\mathrm{gt}}} \tag{30}$$

where ϕ_{ol} and C_{ol} are the volume fraction and water content of olivine, ϕ_{gt} and C_{gt} are the volume fraction and water content of garnet, and $C_{\mathrm{o/g}}$ is the water content of the combined olivine and garnet modes (dashed grey line in Fig 6a). We follow the same procedure for the pyroxenes

$$C_{\mathrm{pyx}} = \frac{\phi_{\mathrm{opx}} C_{\mathrm{opx}} + \phi_{\mathrm{cpx}} C_{\mathrm{cpx}}}{\phi_{\mathrm{opx}} + \phi_{\mathrm{cpx}}} \tag{31}$$

where C_{pyx} is the water content of the combined orthopyroxene and clinopyroxene modes (solid grey line in Fig 6a).

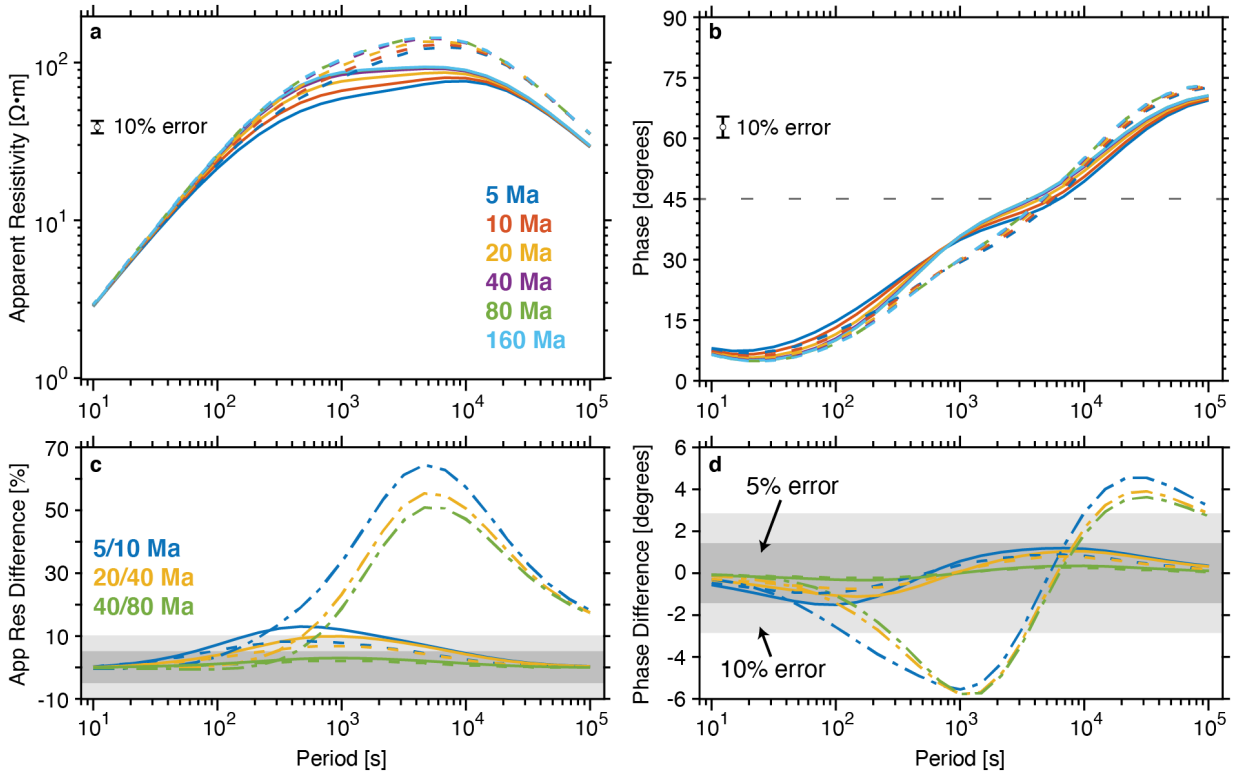

Figure 5: *MT responses as a function of period for dry oceanic mantle. (**a**) Apparent resistivity and (**b**) phase. Line colors correspond to plate age geotherms from Fig 4b. Solid and dashed lines are 1420°C MPT and 1350°C MPT, respectively. Relative differences between (**c**) apparent resistivity and (**d**) phase responses. Solid and dashed line colors represent the differences between the 5 and 10 Ma (blue), 20 and 40 Ma (yellow), and 40 and 80 Ma (green) plate responses at the same MPT. Dash-dot line colors represent the response differences between the two MPTs at 5 Ma (blue), 20 Ma (yellow), and 80 Ma (green). Dark and light grey boxes are the 5% and 10% equivalent errors, respectively.*

Lastly, we apply the HS^+ mixing model (Eq. 19) to calculate the bulk EC for the 10 Ma and 40 Ma geotherms (1350°C MPT; Fig 6b). Since the effect of water on the EC of NAMs is described by several competing models, we apply the endmember empirical relationships to give two contrasting EC trends for the same hydration level that represent an estimate of the uncertainty. The conductive endmember uses W06 for olivine and D09b for pyroxene (EC model naming convention corresponds to Fig 2 legend). The resistive endmember uses Y09 for olivine and Z12 for pyroxene. Both are presented in Figure 6c. Although no comparison is shown, they are similar to the endmember models (solid red and blue curves) in Fig 3 that included garnet in their mixtures. We note that for the olivine water contents considered here (<100 ppm), the Y09 and S19 olivine resistivity predictions are nearly identical (see Fig 2a). Figure 7 shows the corresponding MT responses.

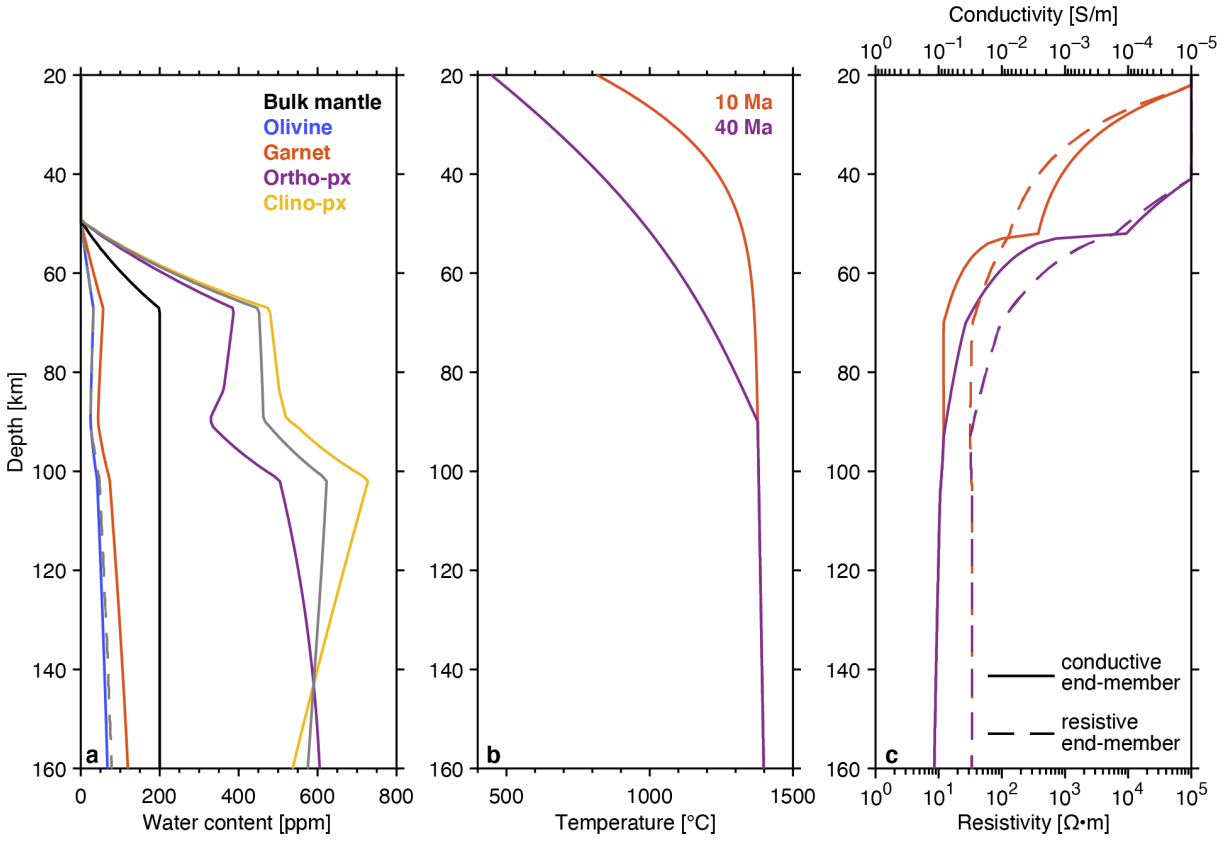

Figure 6: ***(a)*** *Water content distribution in oceanic mantle peridotite. Black line is the bulk mantle water content. Colored lines show water in each mineral phase. Grey dashed and solid lines are the water in olivine and water in pyroxene calculated with Eq 30 and Eq 31, respectively.* ***(b)*** *Oceanic plate geotherms for 1350°C MPT at 10 and 40 Ma.* ***(c)*** *Predicted bulk mantle EC based on temperature and water content in panels* ***(a)*** *and* ***(b)****.*

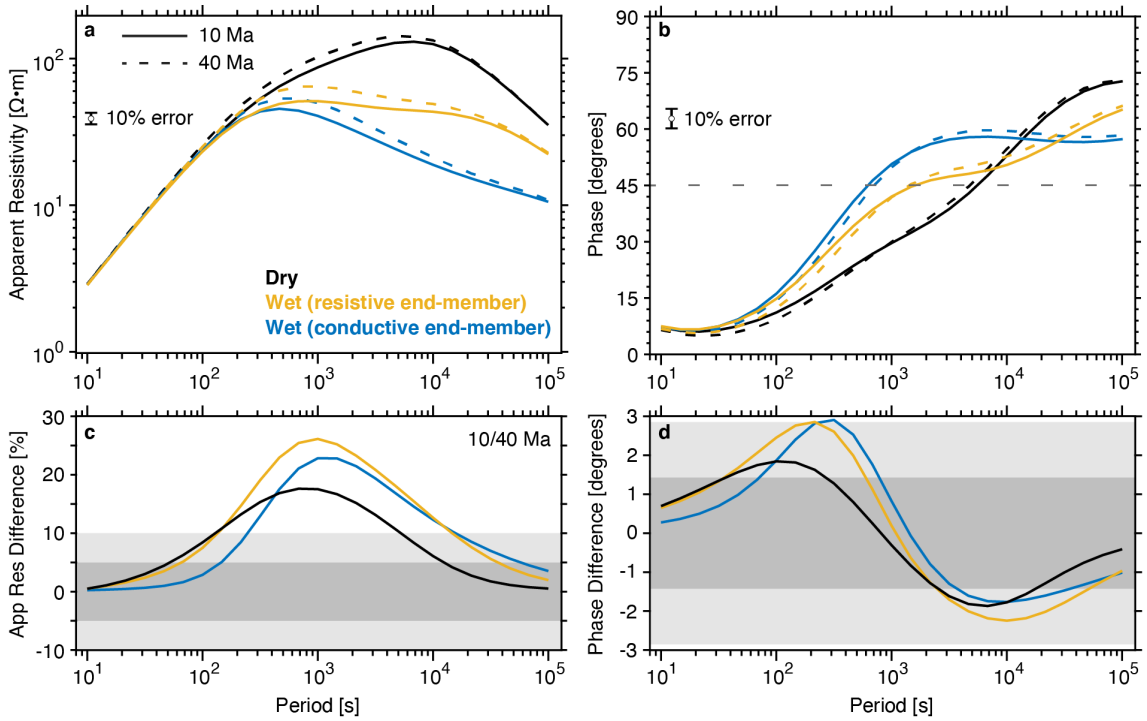

Figure 7: *MT responses as a function of period for hydrated oceanic mantle. (**a**) apparent resistivity and (**b**) phase. Solid and dashed lines correspond to 10 Ma and 40 Ma plate geotherms (1350°C MPT), respectively. Relative differences between (**c**) apparent resistivity and (**d**) phase responses. Line colors represent the response differences between 10 and 40 Ma for dry (black), resistive endmember (yellow), and conductive endmember (blue). The differences between dry, resistive endmember, and conductive endmember responses are not shown since they are significantly larger than typical data errors. Dark and light grey boxes are the 5% and 10% equivalent errors, respectively.*

The endmember responses differ significantly from each other and their dry mantle counterpart. This clearly demonstrates that MT data can easily differentiate between dry resistive mantle and damp conductive mantle regardless of the discrepancy between hydrous mineral EC models. Although the effect of 10 vs 40 Ma plate on the responses is notably less than the contrast between dry and damp mantle or between damp endmember models, it is still larger than typical data errors. In practice, temperature is also an important source of uncertainty, but the magnitude of this uncertainty is not enough to misconstrue dry and damp mantle (see Fig 3). However, this example also demonstrates remarkably different responses between the hydrous mantle endmember models for what is ultimately the same prescribed water content. The same is true in reverse, inferring water contents from MT is highly dependent on endmember model choice and thus has large uncertainties. The disagreement is significant enough that it can lead to contradictory interpretations on whether parts of the asthenosphere are hydrated or contain partial melt (Wang et al., 2006; Yoshino et al., 2006; Naif, 2018; Selway & O'Donnell, 2019), which is fundamental to understanding the drivers of plate tectonics. This is precisely why it is so critical to resolve the discrepancies between laboratory studies.

4.1.3 Partially molten mantle

When the mantle undergoes melting, water has a strong affinity for and readily partitions into the melt phase. This process extracts nearly all of the water and essentially dries out the surrounding mantle rock. The melt is also several orders of magnitude more conductive than the solid matrix and can be interconnected even at very small melt fractions (e.g., Zhu et al., 2011; Gardés et al., 2020). As a result, the bulk EC is dominated by the volume fraction, interconnectivity, and volatile concentration of the melt.

We consider four partial melt models for a 20 Ma plate. We apply the HS+ (Eq. 19) to calculate the bulk EC. For the solid mantle phase (σ_r), we use the 20 Ma dry mantle EC from Fig 4c. For the melt phase (σ_c), we calculate the EC with Eq. 16 for basaltic melt having 2 wt% H_2O. The first and second models add 1 vol% hydrous partial melt to 60–120 km and 60–80 km depths, respectively. Since MT data are better at constraining the conductance than at resolving the EC with depth, the third and fourth models use the same conductance as the 60–120 km melt layer (~8.4 S) distributed over a 20 km thick (60–80 km depth) and 40 km thick (60–100 km depth) layer. The MT responses are shown in Fig 8.

We intentionally consider partial melt models that have bulk EC predictions comparable to the wet conductive endmember model over the depth interval where melt was added. As expected, the partial melt and hydrous mantle MT responses look similar at periods less than 1000 s. However, differences in the phase are noticeable due to the sharp jump in EC at 60 km depth, where the transition from dry mantle to 1 vol% melt occurs. At longer periods, the MT fields have increasing sensitivity to the dry resistive mantle below the melt channel, hence the partial melt model responses steer back towards the dry mantle model response. If we elected to assume the mantle below the melt channel was hydrated and assigned the conductive endmember values, the partial melt and wet conductive endmember model responses would more closely resemble one another. This example demonstrates why interpreting MT data is nonunique. Multiple candidate mechanisms can be invoked to enhance EC and explain the observations. In practice, distinguishing between partial melt, hydration, and temperature interpretations is much more likely when independent geological, petrological, geochemical, and geophysical constraints are available for synthesis. In addition, a growing number of olivine EC measurements are significantly more resistive than W06, which suggests that the conductive endmember model here is anomalous and the resistive endmember is a better predictor of hydrated mantle EC. In that case, the capacity to arrive at a unique solution is further improved since mantle water content alone would not be able to explain high conductivity observations.

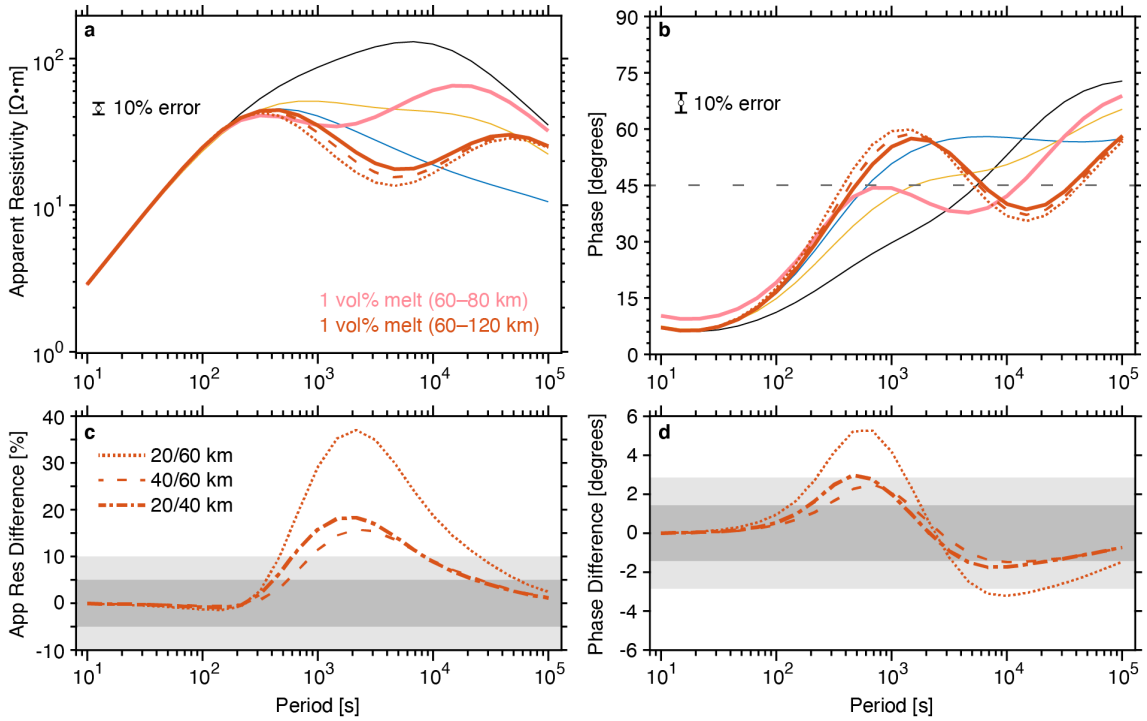

Figure 8: *Comparison of MT responses for 20 Ma oceanic plate (1350°C MPT). (**a**) apparent resistivity and (**b**) phase. Thin solid lines show responses for dry (black) and 200 ppm H_2O mantle (resistive endmember in yellow, conductive endmember in blue). Solid pink and solid red lines are the responses for 1 vol% hydrous basaltic melt added to 60–80 km depth and 60–120 km depth, respectively. The dashed and dotted red lines use the same conductance as the 60 km thick melt layer but distributed over a 20 km thick (60–80 km depth) and 40 km thick layer (60–100 km depth), respectively. Relative response differences in (**c**) apparent resistivity and (**d**) phase between the three models with equivalent melt layer conductance. The differences between dry, damp endmembers, and melt model responses are not shown since they are significantly larger than typical data errors. Dark and light grey boxes are the 5% and 10% equivalent errors, respectively.*

4.2 Continental Mantle

In contrast to oceanic settings, the continental lithosphere is complex and highly heterogeneous. We forward modelled the MT responses for predicted EC of continental lithosphere of various compositions and geotherms. The topmost layer is 0.5 km thick and 50 Ω·m. For the crust, we used a 'wet' composition, following the model of Selway (2018). This model consists of 10 vol% amphibole throughout the crust (conductivity from Wang et al., 2012) and petrologically constrained modal proportions of orthopyroxene (conductivity from Yang et al., 2012), clinopyroxene (conductivity from Yang et al., 2011), quartz (conductivity from Wang et al., 2010) and feldspar (conductivity from Yang et al., 2012). This crustal composition is highly resistive (>10^4 Ω·m) as it does not contain any conductive phases such as pore fluids or graphite.

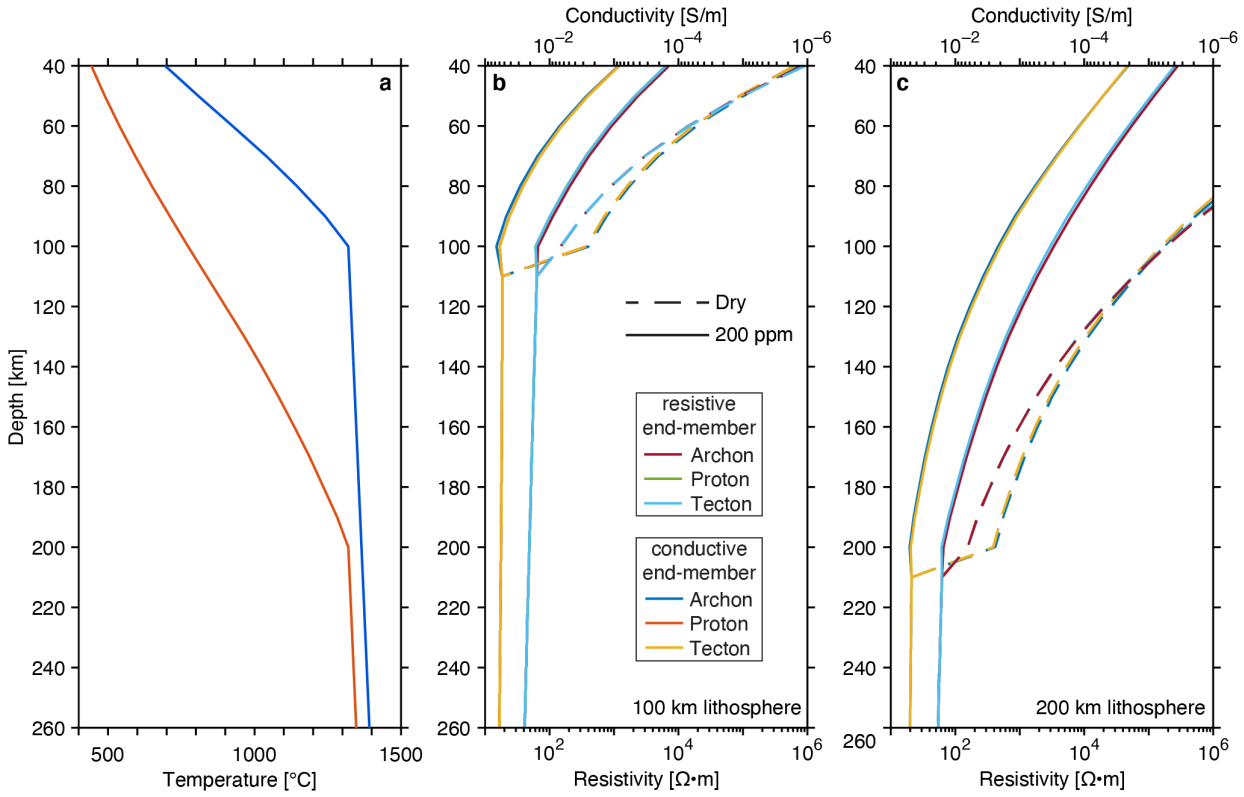

Figure 9: *Resistivity structure of simplified continental upper mantle. (**a**) Geotherms for 100 km and 200 km thick lithosphere. Predicted resistivity-depth profiles for (**b**) 100 km thick lithosphere and (**c**) 200 km thick lithosphere modelled with both dry and 200 wt ppm H_2O peridotite compositions and modal mineralogies of Archon, Tecton, and Proton bulk compositions. The conductive endmember uses the W06 olivine conductivity formulation and the D09b pyroxene formulation, while the resistive endmember uses Y09 and Z12.*

For the lithospheric mantle, we used the xenolith-derived Archon, Proton, and Tecton modal compositions of Griffin et al. (2009), where Archon lithosphere has been stable since >2.5 Ga and is composed of 88 vol% olivine, 11 vol% orthopyroxene, and 1 vol% garnet; Proton lithosphere experienced tectonism at 2.5-1 Ga and is composed of 68 vol% olivine, 20 vol% orthopyroxene, 5 vol% clinopyroxene, and 7 vol% garnet; and Tecton lithosphere was formed or modified after 1 Ga and is composed of 62 vol% olivine, 12 vol% orthopyroxene, 12 vol% clinopyroxene, and 14 vol% garnet. The conductivity calculations for these models and the mixing models used to combine them were the same as for the oceanic mantle. For the asthenospheric mantle, we calculated modal proportions of olivine, pyroxene, and garnet from the formulations of Hirschmann et al. (2009), as was done for the oceanic mantle models.

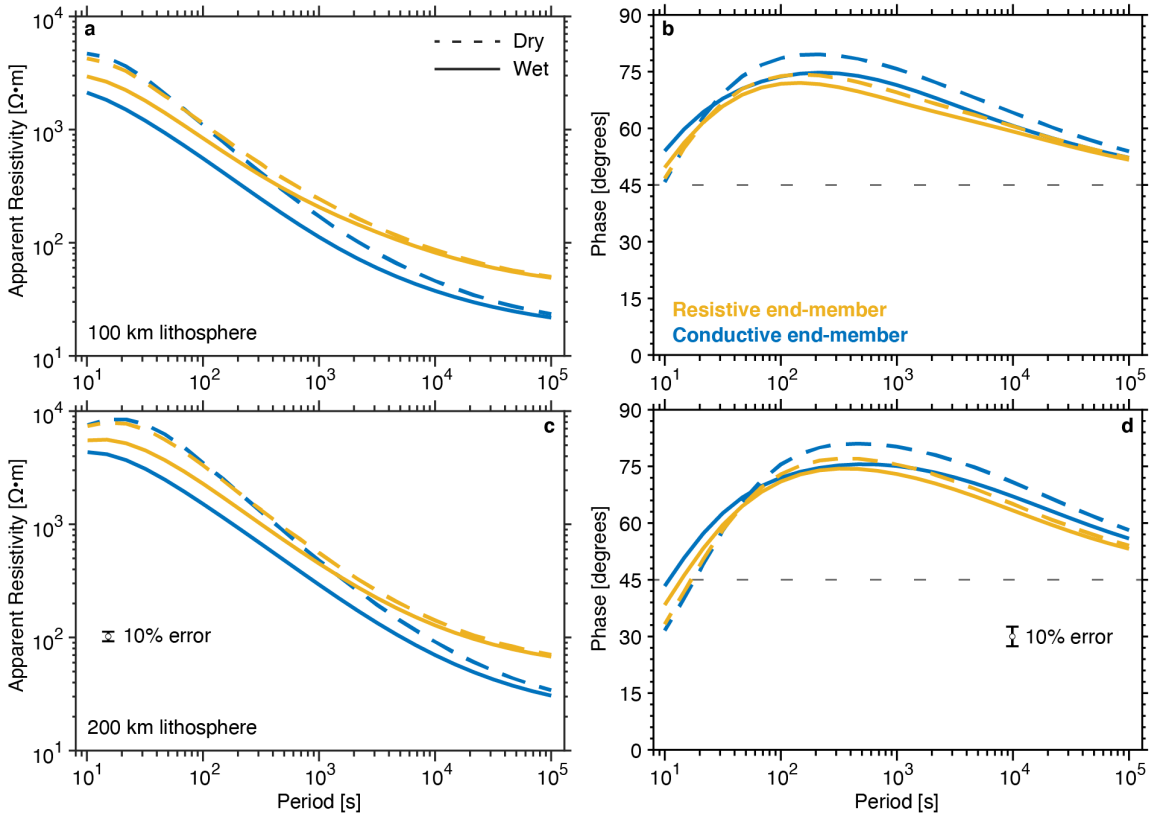

Figure 10: *Forward modelled MT sounding curves for lithosphere with both dry and wet (200 wt ppm H_2O) peridotite compositions. (**a**) Apparent resistivity and (**b**) phase for 100 km thick lithosphere. (**c**) Apparent resistivity and (**d**) phase for 200 km thick lithosphere. While the difference between dry and wet responses is measurable, the differences in the sounding curves between Archon, Tecton, and Proton compositions are smaller than the thickness of the lines and hence unresolvable in real data.*

Models were run for lithospheric thicknesses of 100 and 200 km with crustal thicknesses of 20 and 30 km, respectively. Steady-state lithospheric geotherms were calculated using standard models (Jaupart et al., 2007) with mantle heat production of 2 x 10^{-8} mW/m^3. The asthenospheric adiabat was set at 0.45 K/km (Katsura et al., 2010). All lithospheric mantle models were run at dry conditions and with a total peridotite water content of 200 wt ppm, while the asthenosphere water content was set to 200 wt ppm in all models. Hydrous models were run using both the conductive and resistive endmember empirical conductivity laws, and hydrogen partitioning between minerals was calculated via the partition coefficients of Hirschmann et al. (2009) and O'Leary et al. (2010), as was done for the oceanic mantle models. Figure 9 shows the temperature and EC predictions for upper mantle with dry and wet lithosphere, and Figure 10 shows the corresponding MT responses.

All results show that the changes in modal proportions between Archon, Tecton, and Proton mantle produce minor differences in the bulk EC and thus in the MT responses as well, at least for the mixing model and water partitioning considered here (see Özaydin & Selway

(2020) for compositional effects on EC with different mixing models and water partitioning). In contrast, the addition of water produces a measurable decrease in AR and in the gradient of the phase curve. Since the resistive endmember predicts that water has a smaller effect on olivine conductivity, these models show a concomitantly smaller decrease in apparent resistivity. All AR curves have a general decreasing trend, although the models with 200 km thick lithosphere show a peak in AR at a period of ~20 s whereas the AR for 100 km thick lithosphere models peaks at a shorter period than shown here. Per the skin depth approximation (Eq. 26), this is because the 200 km thick lithosphere models remain highly resistive to greater depths and as a result the MT data begin to sense the deeper conductive mantle at longer periods relative to the 100 km thick lithosphere models.

The models with a 200 km thick lithosphere have higher AR than those with 100 km thick lithosphere at all but the longest periods (greater than $\sim 10^4$ s). The phase data show clear differences between the lithospheric thickness models. All phase curves show a peak of ~70–80 degrees at a period of several hundred seconds. At shorter periods the resistivity increases with depth as the MT signals move from the lower crust to the uppermost mantle. The peak occurs where the gradient in AR curves is strongest in the uppermost mantle before flattening out in the deeper lithosphere and asthenosphere. As noted earlier, this peak is of higher magnitude and occurs at longer periods in the 200 km thick lithosphere models due to the greater depth extent of the highly resistive mantle. Apparent resistivities in the resistive endmember models decrease more homogeneously in the lithospheric mantle, leading to flatter phase curves. In the adiabatic geotherm of the asthenosphere, the AR curves decrease more slowly, leading to lower phase values.

We also considered the impact of asthenospheric partial melt on continental MT sounding curves. For simplicity, we only considered carbonated melt since carbon-free melt is unlikely to be thermodynamically stable to an extensive depth range beneath continental lithosphere (Hirschmann, 2010). We added 1 vol% carbonated melt to our previously computed peridotite compositions, which were fixed at 200 wt ppm water. Because the water in mantle minerals will preferentially partition into the melt phase and the addition of water to the melt enhances its EC, we used the partitioning relationships of Hirschmann et al. (2009) to estimate the water content in the melt. Calculations were made for dry and 200 wt ppm water with Proton lithosphere compositions for both 100 and 200 km lithospheric thicknesses, using the experimental conductivity formulations of the resistive and conductive endmembers, as was done for hydous melt-free mantle.

All results show similar trends and show that the decrease in asthenospheric resistivity caused by the interconnected melt has a strong effect on the MT responses (Fig 11). The AR values for the melt-bearing models are the same as the melt-free models at periods less than a few hundred seconds, where the signals have not penetrated into the asthenosphere. At longer periods, the AR values for the melt-bearing models decrease more sharply than the melt-free models. The melt-bearing AR curves of the resistive and conductive endmember

models also converge at the longest periods since the bulk resistivity of the asthenosphere is dominated by the melt resistivity even at a melt fraction of only 1 vol%. However, the AR is lower for the models with 100 km thick lithosphere than those with 200 km lithosphere since more of the signal is penetrating into the asthenosphere. Phase values for the melt-bearing models are higher than the melt-free models at periods longer than a few hundred seconds since the imaged resistivity is decreasing more sharply with depth. The difference between wet and dry lithosphere models is more pronounced for the conductive endmember formulation due to the larger influence of water on conductivity.

5. Discussion

5.1 Oceanic Mantle

Oceanic plates are continuously being regenerated and recycled at plate boundaries, and the very process that gives birth to oceanic lithosphere at mid-ocean ridges is fairly uniform as exemplified by narrow range of observed crustal thicknesses globally (White et al., 1992). Unsurprisingly, the oceanic lithosphere-asthenosphere system is considered to be "simple," having a relatively well-defined composition and 1D layered structure where temperature (plate age) is the dominant variable that modulates the rheology. Yet there is still no consensus on the origin of the low viscosities in the asthenosphere. While on average oceanic lithosphere is indeed younger and less modified than continental lithosphere, a growing number of observations either invoke mechanisms other than temperature to explain geophysical observations and/or show a much more complex and dynamic system than originally thought (e.g., Beghein et al., 2014; Kawakatsu & Utada, 2017). This is certainly also reflected in marine MT observations.

Figure 12 shows the MT responses and Figure 13 shows the dry mantle temperature vs. water content vs. partial melt fraction required to explain the modelled EC observations from 3 Ma (Evans et al., 2005), 23 Ma (Naif et al., 2013), 70 Ma (Sarafian et al., 2015), and 130 Ma (Baba et al., 2013) oceanic plates. We calculate the dry mantle temperatures following the methodology in Section 4.1.1. These temperature estimates often exceed the plate cooling model geotherms. Alternatively, we adopt the expected temperatures from the plate cooling model geotherms and use them to calculate either the water content or the partial melt fraction that matches the observations. For the hydration estimates, we follow Section 4.1.2 and consider both the resistive and conductive endmember EC laws as well as both the 1350°C and 1420°C MPT geotherms. As expected, the results exhibit a large discrepancy between the endmembers. For the partial melt estimates, we follow Section 4.1.3 and fix the water content in the melt at 2 wt% H_2O. In practice, this water content depends on the hydration state of the mantle where the melt was formed as well as the degree of melting.

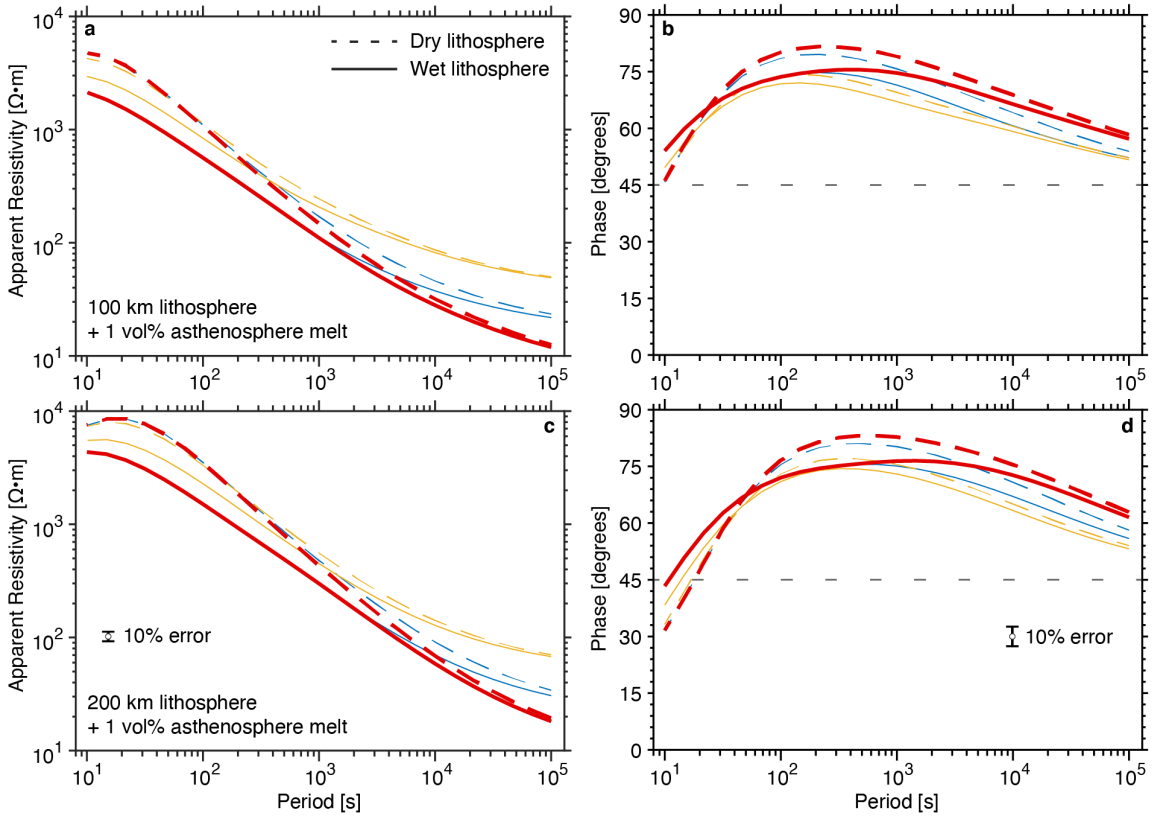

***Figure 11**: Forward modelled MT sounding curves for melt-bearing asthenosphere with dry and damp lithosphere. (**a**) Apparent resistivity and (**b**) phase for 100 km thick lithosphere. (**c**) Apparent resistivity and (**d**) phase for 200 km thick lithosphere. Red lines show 1 vol% asthenospheric melt responses for dry (dashed lines) and 200 wt ppm H_2O mantle (solid lines), respectively. Yellow and blue lines are the melt-free resistive and conductive endmember models from Fig 10. Melt-bearing models with damp mantle were run with the conductive endmember formulation.*

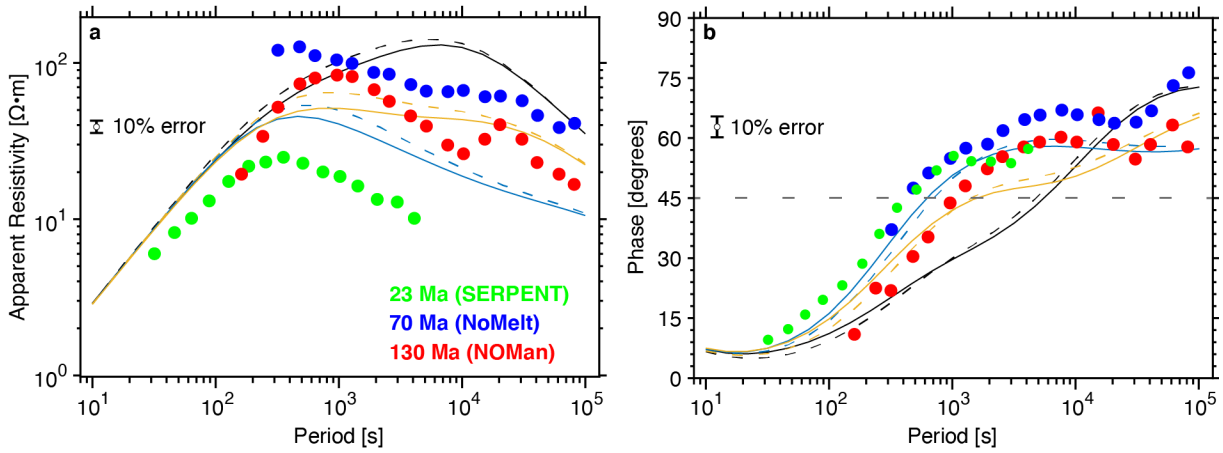

***Figure 12**: Comparison between MT responses from predictions and select seafloor observations. Field examples are from approximately 1D oceanic plate at different ages: 23 Ma Cocos plate (Naif et al., 2013), 70 Ma Pacific plate (Sarafian et al., 2015), and 130 Ma Pacific plate (Baba et al., 2013). Predicted model responses are taken from Fig 7.*

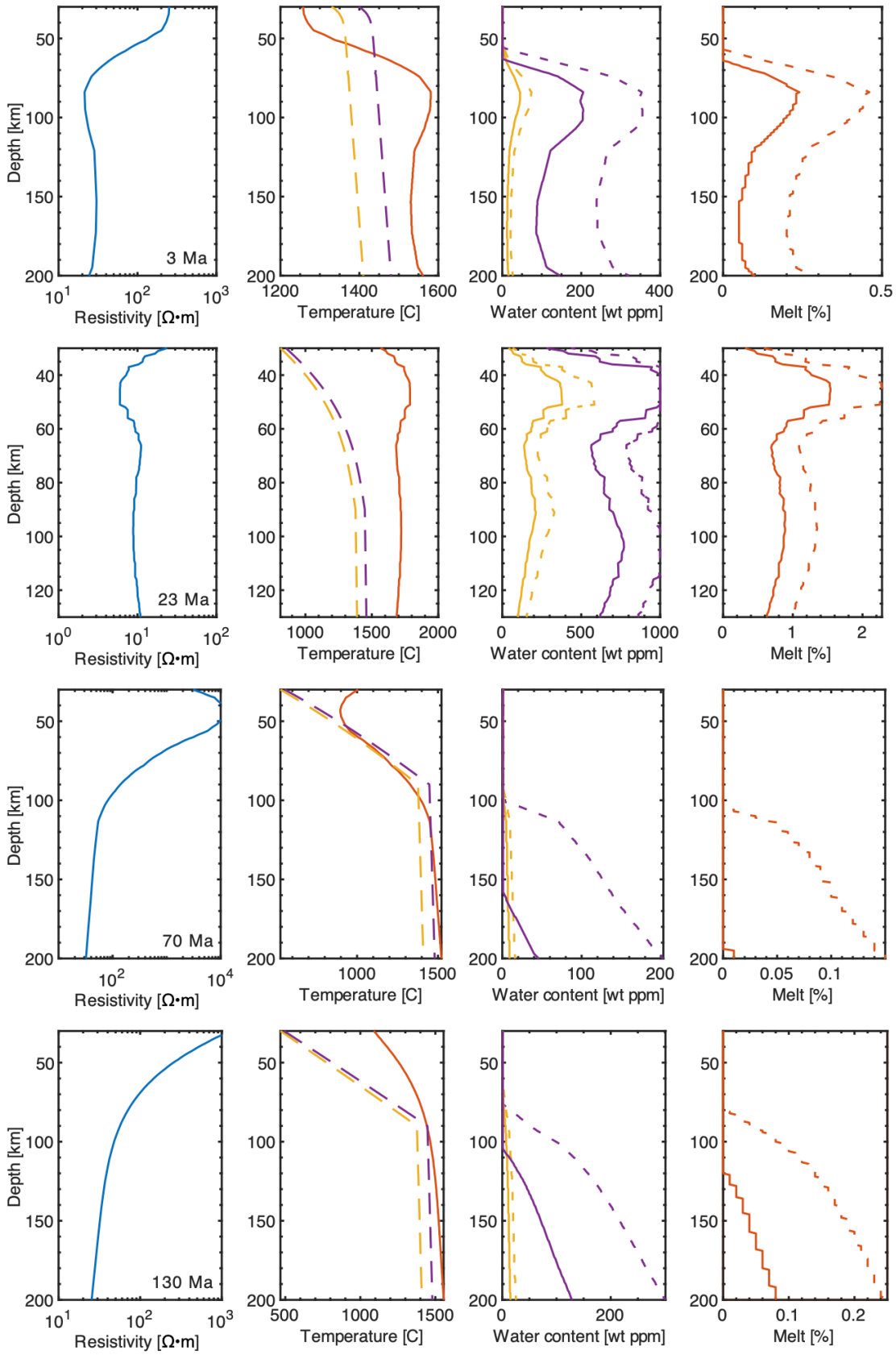
Depth [km]
3 Ma
Resistivity [Ω•m]
Temperature [C]
Water content [wt ppm]
Melt [%]
23 Ma
70 Ma
130 Ma

972

Figure 13: *The first column panels show the resistivity observations. The second column panels show the dry mantle temperature required to explain the observations (red lines) and compares them against the expected temperature from plate cooling models for both 1350°C (green dashed lines) and 1420°C MPT (blue dashed lines). The third column panels show the water contents that explain the observations estimated with the resistive endmember formulation (blue lines) and conductive endmember formulation (green lines) for both the 1350°C MPT (dashed lines) and 1420°C MPT geotherm (solid lines). The fourth column panels show the melt fraction required to explain the observations for the 1350°C MPT (dashed lines) and 1420°C MPT geotherm (solid lines).*

The results for the 23 Ma plate provide an example where a unique interpretation exists. This is because the dry solid-state mantle temperature estimates are so high that they exceed the dry solidus and would induce melting. Similarly, the water content estimates are so high that they exceed the hydrated solidus and would also induce melting (Naif et al., 2013; Naif, 2018). Therefore, partial melt is required. The remaining observations are nonunique and need additional independent constraints. For example, the results for the 3 Ma plate are nonunique in the 1350°C MPT geotherm case; the dry mantle temperature and the 1420°C MPT water content estimates exceed the dry and hydrated solidus, respectively, thereby requiring melt. However, both the MT and collocated seismic observations there suggest that melting beneath the ridge axis—where the plate is 0 Ma—extends to at least 100 km depths (Forsyth et al., 1998; Baba et al., 2006). In order for melt production to extend that deep, the MPT must be larger than 1350°C or the mantle must be highly hydrated, both of which point to a partial melt interpretation (Naif, 2018). The observations for the 70 and 130 Ma plates are fully nonunique and can be attributed to either slightly elevated temperatures (dry mantle case), nearly dry mantle (conductive endmember case), a reasonable water content that is consistent with MORB estimates (resistive endmember case), or a very small melt fraction (<<1%) (Sarafian et al., 2015; Naif, 2018).

5.2 Continental mantle

One of the most striking discoveries about the continental lithospheric mantle over the past few decades has been its electrical complexity. From early lithosphere-scale surveys such as Lithoprobe in Canada (e.g., Jones et al., 2005) to recent continent-scale arrays such as USArray, SinoProbe, and AusLAMP (e.g., Dong et al., 2013; Meqbel et al., 2014; Robertson et al., 2016; 2020), MT models show that conductivity contrasts of orders of magnitude exist within continental lithospheric mantle that might have otherwise been thought to be homogenous.

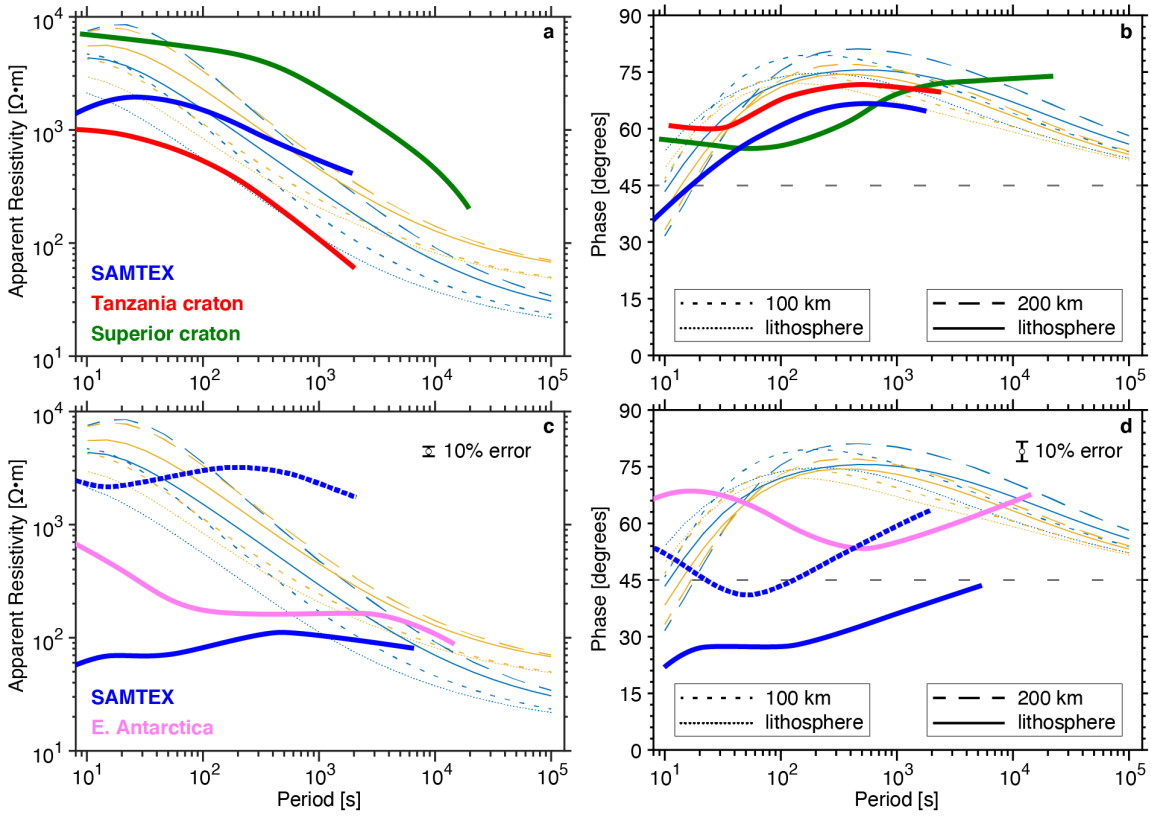

Figure 14: *Comparison between predicted and observed MT sounding curves. (**a**) Apparent resistivity and (**b**) phase for examples from approximately 1D cratonic regions in the Tanzanian craton (Selway, 2015), southern Africa (SAMTEX dataset, Jones et al., 2009), and the Superior craton (USArray dataset, Yang et al., 2015), which show broadly similar patterns to the forward modelled theoretical curves (yellow/blue lines). (**c**) Apparent resistivity and (**d**) phase for examples for alternate examples from approximately 1D, cratonic regions in southern Africa (SAMTEX dataset, Jones et al., 2009) and East Antarctica (Station B22, Wannamaker et al., 2017), which show strongly contrasting patterns to the forward modelled theoretical curves.*

A comparison between the MT forward models produced for expected standard compositions and real MT data from various parts of the world highlights this observation. In some regions, MT sounding curves approximately match the forward models, with generally decreasing values of apparent resistivity with period and phase curves with a peak between 100 and 1000 s period (Fig 14a-b). Differences between these results and the forward modelled curves produced from standard lithospheric models could be attributed to slight changes in geotherm or hydration. However, most sounding curves from the real Earth show very little similarity to those calculated in the forward models (Fig 14c-d) and suggest substantial deviations from the standard lithospheric models. All sounding curves chosen for this comparison were from cratonic regions, where geochemical and seismic data (Griffin et al., 2009) would suggest the continental lithospheric mantle is at its most homogenous. Additionally, their MT responses suggest an approximately 1D, or horizontally

1027 layered, Earth resistivity model. Even in these settings, the MT data show that the continental
1028 lithospheric mantle is much more complex than suggested by simple predictions.

1029 The differences between the forward modelled and observed continental MT data have
1030 several plausible explanations. Some of these relate to crustal complexities not included in
1031 our forward models. Near-surface features can cause galvanic distortion of the EM fields
1032 being measured by the MT method, including a frequency-independent 'static shift' that
1033 causes the apparent resistivity values to be offset up or down the vertical axis (e.g., Jones,
1034 2012). This could explain, for instance, the relatively low magnitude of the apparent
1035 resistivity values in the Tanzanian craton compared to the forward models (Fig 14a-b), but
1036 it is not able to explain differences between the observed and modelled phases or the
1037 contrasting shapes of the apparent resistivity curves shown in Fig 14c-d. The crustal
1038 composition used in our forward model was simple and of high resistivity, containing some
1039 amphibole but otherwise composed of anhydrous minerals, and not containing any strongly
1040 conductive phases like graphite or pore fluids. In contrast, many crustal regions worldwide
1041 have anomalously low resistivities (e.g., Jones & Ferguson, 2001). This has an effect on
1042 mantle MT models since the depth penetration of an MT signal is dependent on both the
1043 period of the signal and the resistivity of the Earth. Therefore, if the crust is more conductive
1044 in the regions shown in Fig 14 than in our forward model, the MT signals at a given period
1045 will be imaging a shallower depth than in our forward model response.

1046 The most important reason that the observed continental MT data differ from the forward
1047 models is that, even in stable continental lithosphere, the Earth is more complex than the
1048 models. Significant conductors and lateral heterogeneity have been found in every craton
1049 that has been imaged with MT (e.g., Jones et al., 2003; Thiel et al., 2005; Padilha et al., 2006;
1050 Jones et al., 2009; Yang et al., 2015). In some regions, the magnitude of these conductors is
1051 such that they could reasonably be caused by high water contents in standard, nominally
1052 anhydrous mantle minerals (e.g., the Tanzanian craton; Selway, 2015). However, in other
1053 regions, these conductors are of such a large magnitude that they cannot be explained by
1054 petrologically plausible water contents and must indicate the presence of graphite or other
1055 highly conductive phases (e.g., Jones et al., 2003; Bedrosian, 2016; Wunderman et al., 2018),
1056 or possibly rock deformation (e.g., Pommier et al., 2018).

1057 Most continental evolution models predict neither high water contents nor significant
1058 volumes of highly conductive minerals in the lithospheric mantle. However, these models
1059 were mostly developed before extensive MT images of the continental lithosphere were
1060 available. Seismic tomography models, which have been instrumental in developing our
1061 understanding of the mantle, are not sensitive to water content (e.g., Cline et al., 2018), so
1062 hydrogen-related conductors would not be expected to have a tomographic response.
1063 Continental evolution models propose that the lithosphere should become more dehydrated
1064 as it ages and is subject to melting and depletion events (Griffin et al., 2009). However,
1065 geochemical studies of mantle xenoliths have found that many have unexpectedly high water

contents and that even cratonic mantle is geochemically heterogeneous (e.g., Demouchy & Bolfan-Casanova, 2016), with many regions experiencing extensive metasomatism that could feasibly lead to increased water contents and/or the deposition of conductive minerals. Seismic S-wave receiver functions are sensitive to complexities in the lithospheric mantle including the presence of hydrous minerals, which could cause some conductive anomalies. Like MT, these receiver functions have shown that the continental lithosphere is significantly more complex than previously believed (e.g., Selway et al., 2015). Together, these geochemical and geophysical datasets show that traditional models of continental evolution are too simplistic. Updated continental evolution models should take advantage of the insights offered by MT, especially since many of the features imaged in MT models are invisible to other methods.

5.3 Case Study: MT Constraints on Thermal Lithospheric Thickness in the Southeastern United States

Here we consider a specific example of the value of MT mantle imaging in a continental setting. Given the multiple factors that control EC in the mantle as well as the intrinsic uncertainties in laboratory-derived EC laws (see Section 2.3), it is often difficult to obtain useful upper mantle temperature estimates from MT data alone. However, in certain situations, MT imaging can provide a very strong constraint on temperature, and the resulting bounds may be more robust than those derived from seismic methods. Generally, such situations arise when imaged resistivity values fall within the high-resistivity upper limit of observable values.

As shown in Figure 3, dry mantle mineral conduction laws form an upper bound on how resistive the upper mantle can be as a function of temperature. Consequently, an observed resistivity value provides an upper limit on mantle temperature; any amount of hydration would only lower the temperature inferred from the observed conductivity value. Additionally, while the dry EC laws for all volumetrically significant upper mantle minerals may differ slightly, the magnitude of the difference is too small, at least in the case of dry subcontinental mantle, for the MT data to be able to discern between those laws (see Section 4.2). Therefore, this upper bound on temperature can be established regardless of the details of mineralogy and composition, although its usefulness is limited to regions of the mantle hotter than ~1000°C since MT data lack sensitivity to highly resistive structures (see Section 4.1.1).

Globally, MT imaging of the mantle lithosphere has shown that bulk resistivity values are often low enough (~100 Ω·m) to require at least some degree of hydration (see Section 5.2). This is because the upper bound temperature derived from such moderate resistivity values are unrealistic and much higher than the temperature bounds placed by other geophysical techniques. Although inferring temperature information from MT imaging has proven to be seldom useful, we can leverage independent constraints on temperature to then provide an estimate on mantle hydration, which is a highly valuable constraint when considering that

seismic methods may be insensitive to water content (e.g., Cline et al., 2018). However, although rare, in some locations the observed upper mantle resistivity values are high enough (>300 Ω·m) to provide valuable constraints on temperature. The southeastern United States (SEUS) is one such region, which has a Tecton-type mantle.

In the SEUS, long-period MT data reveal well-resolved high resistivity values (>300 Ω·m) that extend to great depths beneath the Piedmont and Coastal Plain physiographic provinces (Fig 15; Murphy & Egbert, 2017; Murphy & Egbert, 2019). This unusual, high-resistivity structure has been nicknamed the *Piedmont Resistor* (Murphy & Egbert, 2017). As shown by Figure 3, the high resistivity values here require temperatures <1300°C to at least 200 km depth. As the thermal lithosphere-asthenosphere boundary beneath continents is often taken to be the 1330°C isotherm, the MT results therefore indicate that the thermal lithosphere beneath this portion of the SEUS must be at least 200 km thick (Murphy & Egbert, 2017).

This conclusion appears to be in contradiction with inferences from seismic imaging studies; recovered velocities at ~150-200 km depth that are slightly slow with respect to reference models have motivated an interpretation of <150 km-thick thermal lithosphere in this region (e.g., Schmandt & Lin, 2014; Pollitz & Mooney, 2016; Wagner et al., 2018; Fig. 15). However, in calculating seismic velocity as a function of temperature and depth in this region using different models of anelastic controls on seismic observables, it becomes apparent that the recovered absolute seismic velocities are in fact consistent with the predicted velocities at the cold (<1300°C) temperatures required by the MT data (Fig. 15; Murphy & Egbert, 2019). Therefore, taken together, both the MT and seismic results (surface- and body-wave imaging, attenuation maps, converted wave imaging) support uniformly thick (~200 km) thermal lithosphere beneath the SEUS (Murphy & Egbert, 2019).

It is worth noting that the MT data here effectively constrain the depth to the base of the resistive lithosphere yet poorly constrain the resistivity distribution within the Piedmont Resistor. As discussed in Section 4.1.1, MT imaging often lacks sensitivity to the absolute resistivity value of highly resistive structures (>10^4 Ω·m), so that the inverted values can be substantially increased with essentially no effect on data fit. As the data cannot constrain exactly how high the resistivity values are within this structure, the lower bound on temperature there is also unconstrained. Therefore, the MT data require the 1300°C isotherm to be at least at 200 km depth, but a range of lithospheric geotherms within the Piedmont Resistor would satisfy the data (see Murphy & Egbert, 2019).

The Piedmont Resistor is highly unusual. The constituent lithosphere is more resistive than that observed in some cratonic regions (cf. Sections 4.2 and 5.2), and it is far more resistive than what might be expected for lithosphere that experienced rifting in association with breakup of Pangaea and opening of the Atlantic Ocean in the early Mesozoic (e.g., Attias et al., 2017). Previous geodynamic interpretations for the SEUS based on seismic images alone

have suggested that the lithosphere here was thinned during rifting and that the mantle lithosphere has been subsequently eroded by piecemeal delamination and mantle edge convection over the last ~200 Myr (e.g., Biryol et al., 2016); however, the joint analysis of multiple geophysical datasets described above indicates that the lithosphere in the SEUS is uniformly thick (~200 km) and coherent. Therefore, the lithosphere here appears to have remained largely intact since the opening of the Atlantic Ocean (Murphy & Egbert, 2019).

The modern lithospheric state is likely a direct result of eruption of the Central Atlantic Magmatic Province (CAMP) large igneous province, which is one of the largest recognized in the geologic record (e.g., McHone, 2000). Major, widespread mantle melting associated with formation of the CAMP could have depleted the SEUS mantle to form a thick, coherent block of subcontinental lithospheric mantle that persists today. Figure 15 shows possible mantle temperature and viscosity profiles over time for this region. The initial temperature profile, which reflects mantle potential temperature estimates based on the geochemistry of CAMP basalts (Hole, 2015; Shellnutt et al., 2018), only crosses an approximate "wet" (bulk 100 wt ppm H_2O) solidus at depths less than ~130 km, much shallower than the full depth extent of the Piedmont Resistor. However, a higher bulk water content, as might be expected for pervasively subduction-modified mantle (e.g., Whalen et al., 2015), with water hosted in hydrous phases, could further depress the solidus and permit melt depletion to begin at the greater depths suggested by MT. Alternatively, delamination (e.g., Whalen et al., 2015) may have played some role in facilitating deeper melting. Although trace element geochemistry of CAMP basalts suggests melting dominantly occurred at depths of ~60–70 km (Shellnutt et al., 2018), further study is warranted to critically test for a deep-melting signature in the least evolved CAMP samples. These temperature calculations show that conductive cooling over ~200 Myr would allow the upper mantle to reach a thermal state roughly consistent with what is inferred from these geophysical results.

Melt depletion would render the SEUS lithosphere compositionally buoyant and would also leave the constituent mantle virtually dry. The possible viscosity profiles in Figure 15 demonstrate that removal of water leads to a substantial increase in strength, and this strength could permit the CAMP-depleted mantle to withstand convective destruction at its initial formation and to survive as a rigid block through time. Interestingly, the likely buoyancy and rigidity of this lithosphere has motivated speculation that the Piedmont Resistor may represent a Mesozoic example of craton formation (Murphy & Egbert, 2019), as compositional buoyancy and rheological strength are generally considered to be necessary conditions for long-term lithosphere stability.

These MT-derived insights into lithospheric properties in the SEUS demonstrate the value of EC imaging for studies of the upper mantle, especially in combination with other geophysical techniques. In the SEUS, MT imaging is key to illuminating lithospheric properties and an associated geodynamic story that would remain opaque with seismic imaging alone.

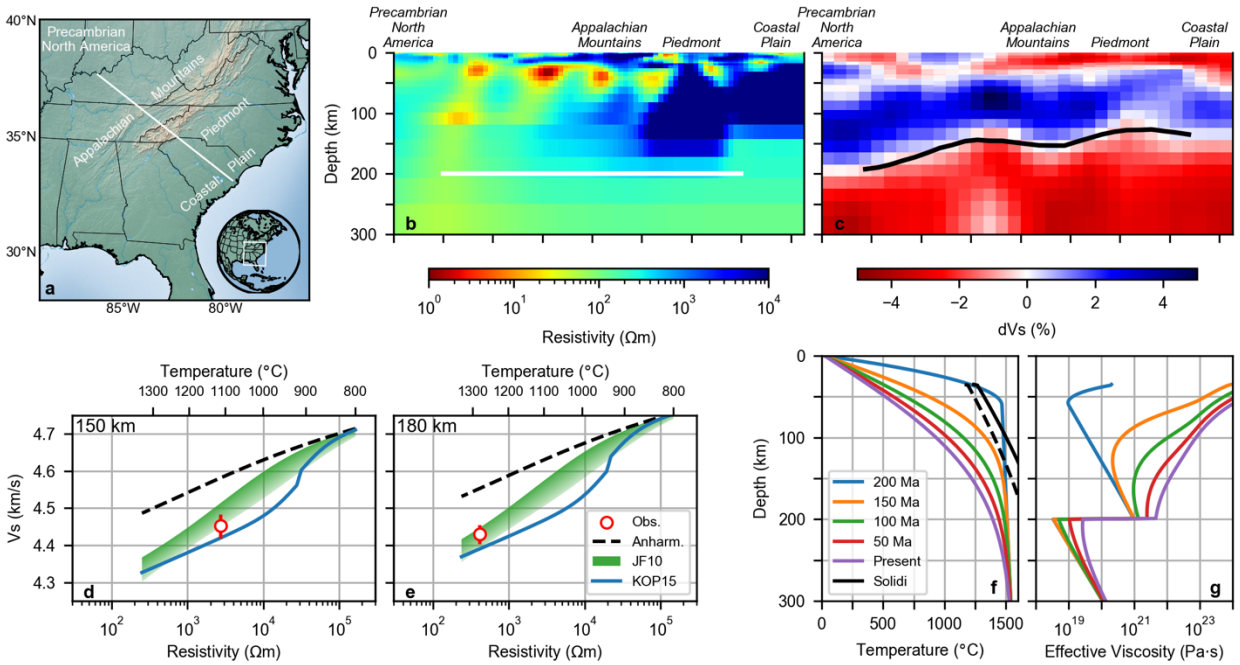

Figure 15: *Southeastern United States (SEUS) case study. (**a**) Overview map with geographic locations and the cross-section profile (white line). (**b**) Resistivity cross section from MT imaging (from Murphy & Egbert, 2019); white line is the inferred thermal lithosphere-asthenosphere boundary (1330°C isotherm). (**c**) Shear-wave velocity cross section from surface wave imaging, expressed as percent difference with respect to 4.5 km/s (from Wagner et al., 2018); black line is the 1330°C isotherm. Horizontal axis tick interval on the cross sections is 100 km. (**d-e**) Comparison of geophysical observations to anelastic predictions (after Murphy & Egbert, 2019). The black dashed line is the purely anharmonic prediction of velocity as a function of temperature (at the specified depth); the green shaded region is the range of anelastic predictions from the model of Jackson & Faul (2010) for grain sizes of 10 cm (dark shading) to 1 mm (light shading); and the solid blue line is the anelastic prediction from the model of Karato et al. (2015) for a grain size of 5 mm. The red dot shows the median resistivity-shear velocity (Vs) pair for observations within the Piedmont Resistor volume at the specified depth (from the two displayed geophysical images); the bars show the full range of Vs values. The one-to-one mapping between resistivity and temperature assumes a dry olivine conduction law (justified by the very high resistivity values within the Piedmont Resistor). The exact matchup between observations and predictions is unimportant, as there are many factors (e.g., the details of mantle mineralogy, the effect of mineral chemistry on Vs) that are ignored here; rather, these plots demonstrate that the anelastic predictions can explain relatively slow shear velocities at the cold temperatures required by the MT data. (**f-g**) Possible temporal evolution of temperature and effective viscosity within the Piedmont Resistor. The temperature calculation assumes purely one-dimensional conduction starting from a mantle potential temperature of 1450°C (Hole, 2015; Shellnutt et al., 2018). Also plotted are a dry peridotite solidus (solid black line; Hirschmann, 2000) and a "wet" peridotite solidus, calculated with the cryoscopic approximation (Hirschmann et al., 2009) for bulk 1000 wt ppm H_2O (dashed black line). The effective viscosity calculations use the OL-WB1/g model of Jain et al. (2019) with dry mantle (1 wt ppm H_2O) within the Piedmont Resistor and "damp" mantle (200 wt ppm H_2O) beneath the Piedmont Resistor.*

6. Conclusions

The electrical conductivity signature of the mantle depends on a confluence of factors, including temperature, composition, the concentration of structurally bound hydrogen (i.e., water content) in nominally anhydrous minerals, the partial melt fraction, and the concentration of volatiles (H_2O+CO_2) dissolved in the melt. We have explored some of the tradeoffs between these factors. We have also explored some of the uncertainties that stem from applying competing empirical EC laws for hydrated mantle minerals and from applying different geometric mixing models. Clearly, these all have the capacity to significantly influence the bulk mantle EC, and a fundamental non-uniqueness therefore exists that further complicates interpretations. These complexities must be taken into account when inferring physical properties from EC observations. Incorporating complementary techniques and independent constraints is necessary to reduce the uncertainty as well as the non-uniqueness. Applying a realistic multi-phase mantle composition and petrology constraints such as the distribution of water is warranted. For example, since the water solubility and the damp solidus for the mantle both provide an upper limit on bulk hydration, in some cases a hydration inference can be ruled out when the amount of water required to explain a bulk mantle EC value exceeds this limit. To that end, resolving the discrepancy between laboratory studies on the EC of hydrated minerals will be critical for accurately quantifying the volatile inventory of the mantle and its regional variability. Although we did not directly consider the effect of petrology uncertainties in, for example, water partitioning values between mantle minerals on the EC predictions, it is important to note that these uncertainties are also relevant. Whether pyroxenes hold 5 or 20 times as much water as olivine will translate to large differences in the bulk mantle water content inferred from EC observations.

MT data must be inverted for EC structure, which has its own set of uncertainties that are also critical to consider. Deterministic inversions provide a qualitative assessment of the uncertainty in the modelled EC structure. Ultimately, Bayesian inversion is necessary to account for data errors and to quantitatively assign confidence levels to interpretations, although this is currently computationally prohibitive in 2D and 3D. The electrical mantle is certainly not everywhere an isotropic 1D layered structure but is regionally heterogeneous and potentially anisotropic. Although geophysical inversion and anisotropy were beyond the scope of our review, we did explore in 1D the sensitivity of MT responses to different mantle physical states. We have shown that MT data are highly sensitive to conductors and therefore (non-uniqueness aside) can effectively constrain the lithosphere thickness, mantle potential temperature, bulk hydration, melt porosity, and other factors that enhance conductivity. MT data are also insensitive to resistors ($>10^4$ Ω·m) when said resistors are bounded by relatively conductive features above and/or below, as is always the case on Earth due to the presence of the asthenosphere and deeper conductive mantle. It is therefore important to

bear in mind that MT inversions may not automatically yield high resistivity values in the lithosphere, whereas CSEM data are sensitive to resistors and complementary in this regard.

Despite these complexities and limitations, we emphasize that EC is currently the *only* geophysically observable quantity that can readily be used as a proxy for mantle hydration, melt volatile content and aqueous fluid salinity. It is also the leading tool for imaging migration pathways and mapping porosity of aqueous fluids and partial melts, among other things. Furthermore, MT does not operate in a vacuum; when integrated with petrology, seismology, and other geochemical and geophysical data, EC observations have demonstrably shown their capacity to yield unique constraints on the structure and composition of the mantle.

Acknowledgements

This work was initiated at a Cooperative Institute for Dynamic Earth Research (CIDER) supported workshop held in Fort Collins (EAR-1135452), May 2017. AP acknowledges support from NSF-CAREER grant 1750746. BSM is supported by a Mendenhall Postdoctoral Fellowship through the U.S. Geological Survey. We thank Phil Wannamaker and an anonymous reviewer for their constructive comments. We also thank Anna Kelbert, Krissy Lewis, Brian Shiro, and Janet Slate for their review of this contribution. SN thanks Kerry Key and the LDEO EM Geophysics Lab for discussions.

References

Aizawa, K., Koyama, T., Hase, H., Uyeshima, M., Kanda, W., Utsugi, M., et al. (2014). Three-dimensional resistivity structure and magma plumbing system of the Kirishima Volcanoes as inferred from broadband magnetotelluric data. *Journal of Geophysical Research: Solid Earth*, *119*(1), 198–215.

Archie, G. E. (1942). The electrical resistivity log as an aid in determining some reservoir characteristics. *Transactions of the AIME*, *146*(01), 54–62.

Arrhenius, S. (1889). On the reaction rate of the inversion of non-refined sugar upon souring. *Z. Phys. Chem.* 4, 226–248.

Attias, E., Evans, R. L., Naif, S., Elsenbeck, J., & Key, K. (2017). Conductivity structure of the lithosphere-asthenosphere boundary beneath the eastern North American margin. *Geochemistry Geophysics Geosystems*, 18(2), 676–696.

Baba, K., Chave, A. D., Evans, R. L., Hirth, G., & Mackie, R. L. (2006). Mantle dynamics beneath the East Pacific Rise at 17 S: Insights from the Mantle Electromagnetic and Tomography (MELT) experiment. *Journal of Geophysical Research: Solid Earth*, *111*(B2).

Baba, K., Tada, N., Zhang, L., Liang, P., Shimizu, H., & Utada, H. (2013). Is the electrical conductivity of the northwestern Pacific upper mantle normal?. *Geochemistry, Geophysics, Geosystems*, *14*(12), 4969–4979.

Becker, K. (1985). Large-scale electrical resistivity and bulk porosity of the oceanic crust, Deep Sea Drilling Project Hole 504B, Costa Rica Rift. In *Initial reports DSDP, Leg 83, Balboa to Balboa, Panama* (pp. 419–427). US Govt. Printing Office; UK distributors, IPOD Committee, NERC, Swindon.

Bedrosian, P.A (2016). Making it and breaking it in the Midwest: Continental assembly and rifting from modeling of EarthScope magnetotelluric data. *Precambrian Research*, 278, 337–361.

Bedrosian, P. A., Peacock, J. R., Bowles-Martinez, E., Schultz, A., & Hill, G. J. (2018). Crustal inheritance and a top-down control on arc magmatism at Mount St Helens. *Nature Geoscience*, *11*(11), 865–870.

Beghein, C., Yuan, K., Schmerr, N., & Xing, Z. (2014). Changes in seismic anisotropy shed light on the nature of the Gutenberg discontinuity. *Science*, *343*(6176), 1237-1240.

Bell, D. R., Ihinger, P. D., & Rossman, G. R. (1995). Quantitative analysis of trace OH in garnet and pyroxenes. *American Mineralogist*, *80*(5–6), 465–474.

Bell, D. R., Rossman, G. R., Maldener, J., Endisch, D., & Rauch, F. (2003). Hydroxide in olivine: A quantitative determination of the absolute amount and calibration of the IR spectrum. *Journal of Geophysical Research: Solid Earth*, *108*(B2).

Biryol, C. B., Wagner, L. S., Fischer, K. M., & Hawman, R. B. (2016). Relationship between observed upper mantle structures and recent tectonic activity across the Southeastern United States. *Journal of Geophysical Research: Solid Earth*, 121, 3393–3414.

Blatter, D., Key, K., Ray, A., Gustafson, C., & Evans, R. (2019). Bayesian joint inversion of controlled source electromagnetic and magnetotelluric data to image freshwater aquifer offshore New Jersey. *Geophysical Journal International*, *218*(3), 1822–1837.

Boullier, A M, & Nicolas, A (1975). Classification of textures and fabrics of peridotite xenoliths from South African kimberlites, *Physics and Chemistry of the Earth*, 9, 467–475.

Brace, W. F., & Orange, A. S. (1968). Electrical resistivity changes in saturated rocks during fracture and frictional sliding. *Journal of geophysical research*, *73*(4), 1433–1445.

Burd, A. I., Booker, J. R., Mackie, R., Favetto, A., & Pomposiello, M. C. (2014). Three-dimensional electrical conductivity in the mantle beneath the Payún Matrú Volcanic Field in the Andean backarc of Argentina near 36.5 S: Evidence for decapitation of a mantle plume by resurgent upper mantle shear during slab steepening. *Geophysical Journal International*, *198*(2), 812–827.

1316 Caricchi, L., Gaillard, F., Mecklenburgh, J., & Le Trong, E. (2011). Experimental determination
1317 of electrical conductivity during deformation of melt-bearing olivine aggregates:
1318 Implications for electrical anisotropy in the oceanic low velocity zone. *Earth and Planetary*
1319 *Science Letters*, *302*(1-2), 81–94.

1320 Chave, A. D., & Jones, A. G. (Eds.). (2012). *The magnetotelluric method: Theory and practice*.
1321 Cambridge University Press.

1322 Chave, A. D. (2012). Estimation of the magnetotelluric response function. *The*
1323 *Magnetotelluric Method: Theory and Practice*, 165–218.

1324 Chesley, C., Key, K., Constable, S., Behrens, J., & MacGregor, L. (2019). Crustal cracks and
1325 frozen flow in oceanic lithosphere inferred from electrical anisotropy. *Geochemistry,*
1326 *Geophysics, Geosystems*, *20*(12), 5979–5999.

1327 Cline II, C.J., Faul, U.H., David, E.C., Berry, A.J. and Jackson, I. (2018). Redox-influenced
1328 seismic properties of upper-mantle olivine. *Nature*, *555*(7696).

1329 Comeau, M. J., Käufl, J. S., Becken, M., Kuvshinov, A., Grayver, A. V., Kamm, J., ... & Batmagnai,
1330 E. (2018). Evidence for fluid and melt generation in response to an asthenospheric
1331 upwelling beneath the Hangai Dome, Mongolia. *Earth and Planetary Science Letters*, *487*,
1332 201–209.

1333 Constable, S., & Roberts, J. J. (1997). Simultaneous modeling of thermopower and electrical
1334 conduction in olivine. *Physics and Chemistry of Minerals, 24(5)*, 319–325.

1335 Constable, S. (2006). SEO3: A new model of olivine electrical conductivity. *Geophysical*
1336 *Journal International, 166(1)*, 435–437.

1337 Constable, S., Key, K., & Lewis, L. (2009). Mapping offshore sedimentary structure using
1338 electromagnetic methods and terrain effects in marine magnetotelluric data. *Geophysical*
1339 *Journal International, 176*(2), 431–442.

1340 Constable, S. (2013). Instrumentation for marine magnetotelluric and controlled source
1341 electromagnetic sounding. *Geophysical Prospecting*, *61*, 505–532.

1342 Constable, S., Orange, A., & Key, K. (2015). And the geophysicist replied: "Which model do
1343 you want?." *Geophysics, 80(3)*, E197–E212.

1344 Cox, C. S., Constable, S. C., Chave, A. D., & Webb, S. C. (1986). Controlled-source
1345 electromagnetic sounding of the oceanic lithosphere. *Nature*, *320*(6057), 52–54.

1346 Dai, L., & Karato, S.-I. (2009a). Electrical conductivity of pyrope-rich garnet at high
1347 temperature and high pressure. *Physics of the Earth and Planetary Interiors*, *176*(1-2), 83–
1348 88.

1349 Dai, L., & Karato, S.-I. (2009b). Electrical conductivity of orthopyroxene: Implications for
1350 the water content of the asthenosphere. *Proceedings of the Japan Academy, Series B*, 85(10),
1351 466–475.

1352 Dai, L., Li, H., Hu, H., & Hui, K. (2012). The effect of chemical composition and oxygen
1353 fugacity on the electrical conductivity of dry and hydrous garnet at high temperatures and
1354 pressures. *Contributions to Mineralogy and Petrology*, *163*, 689–700.

1355 Dai, L., & Karato, S.-I. (2014). High and highly anisotropic electrical conductivity of the
1356 asthenosphere due to hydrogen diffusion in olivine. *Earth and Planetary Science Letters*,
1357 *408*, 79–86.

1358 Dai, L., Hu, H., Jiang, J., Sun, W., Li, H., Wang, M., Vallianatos, F., & Saltas, V. (2020). An
1359 Overview of the Experimental Studies on the Electrical Conductivity of Major Minerals in
1360 the Upper Mantle and Transition Zone. *Materials*, *13*, 408.

1361 Dasgupta, R., Hirschmann, M. M., & Smith, N. D. (2007). Water follows carbon: CO2 incites
1362 deep silicate melting and dehydration beneath mid-ocean ridges. *Geology*, *35*(2), 135–138.

1363 de Groot-Hedlin, C. & Constable, S. (1990). Occam's inversion to generate smooth, two-
1364 dimensional models from magnetotelluric data. *Geophysics, 55(12)*, 1613–1624.

1365 Demouchy, S. and Bolfan-Casanova, N. (2016). Distribution and transport of hydrogen in
1366 the lithospheric mantle: A review. *Lithos*, *240*, 402–425.

1367 Dohmen, R., & Milke, R. (2010). Diffusion in polycrystalline materials: grain boundaries,
1368 mathematical models, and experimental data. *Reviews in Mineralogy and Geochemistry*,
1369 *72*(1), 921–970.

1370 Dong, S. W., Li, T. D., Lü, Q. T., Gao, R., Yang, J. S., Chen, X. H., ... & Zhou, Q. (2013). Progress in
1371 deep lithospheric exploration of the continental China: A review of the
1372 SinoProbe. *Tectonophysics*, *606*, 1–13.

1373 Du Frane, W. L., & Tyburczy, J. A. (2012). Deuterium-hydrogen exchange in olivine:
1374 Implications for point defects and electrical conductivity. *Geochemistry, Geophysics,*
1375 *Geosystems*, *13*(3).

1376 Egbert, G. D., & Booker, J. R. (1986). Robust estimation of geomagnetic transfer
1377 functions. *Geophysical Journal International*, *87*(1), 17–194.

1378 Egbert, G.D. (2011). Magnetotelluric Data Processing, in *Encyclopedia of Solid Earth*
1379 *Geophysics*, H.K. Gupta., Springer.

1380 Egbert, G. D., & Kelbert, A. (2012). Computational recipes for electromagnetic inverse
1381 problems. *Geophysical Journal International*, *189*(1), 251–267.

Evans, R. L., Hirth, G., Baba, K., Forsyth, D., Chave, A., & Mackie, R. (2005). Geophysical evidence from the MELT area for compositional controls on oceanic plates. *Nature*, *437*(7056), 249–252.

Fei, H., Koizumi, S., Sakamoto, N., Hashiguchi, M., Yurimoto, H., Marquardt, K., et al. (2018). Mg lattice diffusion in iron-free olivine and implications to conductivity anomaly in the oceanic asthenosphere. *Earth and Planetary Science Letters, 484*, 204–212.

Fei, H., Druzhbin, D., & Katsura, T. (2020). The Effect of Water on Ionic Conductivity in Olivine. *Journal of Geophysical Research: Solid Earth*, *125*, e2019JB019313.

Ferriss, E., Plank, T., & Walker, D. (2016). Site-specific hydrogen diffusion rates during clinopyroxene dehydration. *Contributions to Mineralogy and Petrology, 171(55)*.

Forsyth, D. W., et al. (1998). Imaging the deep seismic structure beneath a mid-ocean ridge: The MELT experiment. *Science, 280*(5367), 1215–1220.

Frost, B. R. (1991). Introduction to oxygen fugacity and its petrologic importance. *Reviews in Mineralogy and Geochemistry*, *25*, 1–9.

Frost, D. J., & McCammon, C. A. (2008). The redox state of Earth's mantle. *Annual Review of Earth and Planetary Sciences*, *36*, 389–420.

Fullea, J., Muller, M. R., & Jones, A. G. (2011). Electrical conductivity of continental lithospheric mantle from integrated geophysical and petrological modeling: Application to the Kaapvaal Craton and Rehoboth Terrane, southern Africa. *Journal of Geophysical Research: Solid Earth*, *116*(B10).

Gamble, T. D., Goubau, W. M., & Clarke, J. (1979). Magnetotellurics with a remote magnetic reference. *Geophysics*, *44*(1), 53–68.

Gardès, E., Gaillard, F., & Tarits, P. (2014). Toward a unified hydrous olivine electrical conductivity law. *Geochemistry, Geophysics, Geosystems*, *15*(12), 4984–5000.

Gardès, E., Laumonier, M., Massuyeau, M., & Gaillard, F. (2020). Unravelling partial melt distribution in the oceanic low velocity zone. *Earth and Planetary Science Letters*, *540*, 116242.

Ghosh, D. B., & Karki, B. B. (2014). First principles simulations of the stability and structure of grain boundaries in Mg2SiO4 forsterite. *Physics and Chemistry of Minerals*, *41*(3), 163–171.

Glover, P. W., Hole, M. J., & Pous, J. (2000). A modified Archie's law for two conducting phases. *Earth and Planetary Science Letters*, *180*(3-4), 369–383.

Glover, P. W. (2010). A generalized Archie's law for n phases. *Geophysics*, *75*(6), E247–E265.

Grandjean, A., Malki, M., Simonnet, C., Manara, D., & Penelon, B. (2007). Correlation between electrical conductivity, viscosity, and structure in borosilicate glass-forming melts. *Physical Review B*, 75(5), 054112.

Griffin, W.L., O'reilly, S.Y., Afonso, J.C. and Begg, G.C. (2009). The composition and evolution of lithospheric mantle: a re-evaluation and its tectonic implications. *Journal of Petrology*, *50*(7), 1185–1204.

Guo, H., & Keppler, H. (2019). Electrical conductivity of NaCl-bearing aqueous fluids to 900° C and 5 GPa. *Journal of Geophysical Research: Solid Earth*, *124*(2), 1397–1411.

Hamilton, M. P., Jones, A. G., Evans, R. L., Evans, S., Fourie, C. J. S., Garcia, X., ... & SAMTEX MT Team. (2006). Electrical anisotropy of South African lithosphere compared with seismic anisotropy from shear-wave splitting analyses. *Physics of the Earth and Planetary Interiors*, *158*(2-4), 226–239.

Hansen, L. N., Zhao, Y. H., Zimmerman, M. E., & Kohlstedt, D. L. (2014). Protracted fabric evolution in olivine: Implications for the relationship among strain, crystallographic fabric, and seismic anisotropy. *Earth and Planetary Science Letters*, *387*, 157–168.

Hashin, Z., & Shtrikman, S. (1962). A variational approach to the theory of the effective magnetic permeability of multiphase materials. *J. Appl. Phys.*, *33*, 3125–3131.

Hasterok, D. (2013). A heat flow based cooling model for tectonic plates. *Earth and Planetary Science Letters*, *361*, 34–43.

Hauri, E. H., Gaetani, G. A., & Green, T. H. (2006). Partitioning of water during melting of the Earth's upper mantle at H2O-undersaturated conditions. *Earth and Planetary Science Letters*, *248*(3-4), 715-734.

Heise, W., Caldwell, T. G., Bannister, S., Bertrand, E. A., Ogawa, Y., Bennie, S. L., & Ichihara, H. (2017). Mapping subduction interface coupling using magnetotellurics: Hikurangi margin, New Zealand. *Geophysical Research Letters*, *44*(18), 9261-9266.

Hirsch, L. M., & Shankland, T. J. (1993). Quantitative olivine-defect chemical model: insights on electrical conduction, diffusion, and the role of Fe content. *Geophysical Journal International*, *114*(1), 21–35.

Hirschmann, M. M. (2000). Mantle solidus: Experimental constraints and the effects of peridotite composition. *Geochemistry, Geophysics, Geosystems*, *1*(10).

Hirschmann, M. M. (2006). Water, melting, and the deep Earth H2O cycle. *Annu. Rev. Earth Planet. Sci.*, *34*, 629–653.

Hirschmann, M. M., Tenner, T., Aubaud, C., & Withers, A. C. (2009). Dehydration melting of nominally anhydrous mantle: The primacy of partitioning. *Physics of the Earth and Planetary Interiors*, *176*(1-2), 54–68.

Hirschmann, M. M. (2010). Partial melt in the oceanic low velocity zone. *Physics of the Earth and Planetary Interiors*, *179*(1-2), 60–71.

Hirth, G., & Kohlstedt, D. L. (1996). Water in the oceanic upper mantle: implications for rheology, melt extraction and the evolution of the lithosphere. *Earth and Planetary Science Letters, 144(1)*, 93–108.

Hirth, G., & Kohlstedf, D. (2003). Rheology of the upper mantle and the mantle wedge: A view from the experimentalists. *GEOPHYSICAL MONOGRAPH-AMERICAN GEOPHYSICAL UNION*, *138*, 83–106.

Hole, M. J. (2015). The generation of continental flood basalts by decompression melting of internally heated mantle. *Geology*, *43*(4), 311–314. doi: https://doi.org/10.1130/G36442.1

Holzapfel, W. B. (1969). Effect of pressure and temperature on the conductivity and ionic dissociation of water up to 100 kbar and 1000 C. *The Journal of Chemical Physics*, *50*(10), 4424–4428.

Jackson, I., & Faul, U. H. (2010). Grainsize-sensitive viscoelastic relaxation in olivine: Towards a robust laboratory-based model for seismological application. *Physics of the Earth and Planetary Interiors*, *183*(1-2), 151–163.

Jain, C., Korenaga, J, & Karato, S. (2019). Global analysis of experimental data on the rheology of olivine aggregates. *JGR: Solid Earth*, 124, 310–334.

Jarrard, R. D. (2003). Subduction fluxes of water, carbon dioxide, chlorine, and potassium. *Geochemistry, Geophysics, Geosystems*, *4*(5).

Jaupart, C., Mareschal, J.C. and Watts, A.B. (2007). Heat flow and thermal structure of the lithosphere. *Treatise on geophysics*, *6*, 217–252.

Johansen, S. E., Panzner, M., Mittet, R., Amundsen, H. E., Lim, A., Vik, E., et al. (2019). Deep electrical imaging of the ultraslow-spreading Mohns Ridge. *Nature*, *567*(7748), 379–383.

Jones, A.G. and Ferguson, I.J. (2001). The electric moho. *Nature*, *409*(6818), p.331.

Jones, A.G., Lezaeta, P., Ferguson, I.J., Chave, A.D., Evans, R.L., Garcia, X. and Spratt, J. (2003). The electrical structure of the Slave craton. *Lithos*, *71*(2-4), 505–527.

Jones, A.G., Ledo, J., Ferguson, I.J., Farquharson, C., Garcia, X., Grant, N., McNeice, G., Roberts, B., Spratt, J., Wennberg, G. and Wolynec, L. (2005). The electrical resistivity structure of Archean to Tertiary lithosphere along 3200 km of SNORCLE profiles, northwestern Canada. *Canadian Journal of Earth Sciences*, *42*(6), 1257–1275.

Jones, A.G., Evans, R.L., Muller, M.R., Hamilton, M.P., Miensopust, M.P., Garcia, X., Cole, P., Ngwisanyi, T., Hutchins, D., Fourie, C.J.S. and Jelsma, H. (2009). Area selection for diamonds using magnetotellurics: Examples from southern Africa. *Lithos*, *112*, 83–92.

Jones, A. G., Fullea, J., Evans, R. L., & Muller, M. R. (2012). Water in cratonic lithosphere: Calibrating laboratory-determined models of electrical conductivity of mantle minerals using geophysical and petrological observations. *Geochemistry, Geophysics, Geosystems*, *13*(6).

Jones, A. (2012). Distortion of magnetotelluric data: Its identification and removal. In A. Chave & A. Jones (Eds.), *The Magnetotelluric Method: Theory and Practice* (pp. 219–302). Cambridge: Cambridge University Press.

Jones, A. G. (2016). Proton conduction and hydrogen diffusion in olivine: an attempt to reconcile laboratory and field observations and implications for the role of grain boundary diffusion in enhancing conductivity. *Physics and Chemistry of Minerals*, 43(4), 237–265.

Karato, S.-i. (1990). The role of hydrogen in the electrical conductivity of the upper mantle. *Nature*, 347(6290), 272–273.

Karato, S.-i. (2013). Theory of isotope diffusion in a material with multiple species and its implications for hydrogen-enhanced electrical conductivity in olivine. *Physics of the Earth and Planetary Interiors*, 219, 49–54.

Karato, S.-i. (2015). Some notes on hydrogen-related point defects and their role in the isotope exchange and electrical conductivity in olivine. *Physics of the Earth and Planetary Interiors*, 248, 94–98.

Karato, S.-i., Olugboji, T., & Park, J. (2015). Mechanisms and geologic significance of the mid-lithosphere discontinuity in the continents. *Nature Geoscience*, 8, 509–514.

Katsura, T., Yoneda, A., Yamazaki, D., Yoshino, T. and Ito, E. (2010). Adiabatic temperature profile in the mantle. *Physics of the Earth and Planetary Interiors*, *183*(1-2), 212–218.

Kawakatsu, H., & Utada, H. (2017). Seismic and electrical signatures of the lithosphere–asthenosphere system of the normal oceanic mantle. *Annual Review of Earth and Planetary Sciences*, *45*.

Kelbert, A., Meqbel, N., Egbert, G. D., & Tandon, K. (2014). ModEM: A modular system for inversion of electromagnetic geophysical data. *Computers & Geosciences*, *66*, 40–53.

Kelley, K. A., Cottrell, E., & Le Voyer, M. (2019). Water Content of MORBs and the Oceanic Upper Mantle. AGU-FM, 2019, V51I-0163.

Key, K., & Constable, S. (2002). Broadband marine MT exploration of the East Pacific Rise at 9° 50′ N. *Geophysical Research Letters*, *29*(22), 11-1.

Key, K., Constable, S., Matsuno, T., Evans, R. L., & Myer, D. (2012). Electromagnetic detection of plate hydration due to bending faults at the Middle America Trench. *Earth and Planetary Science Letters*, *351-352*, 45–53.

Key, K., Constable, S., Liu, L., & Pommier, A. (2013). Electrical image of passive mantle upwelling beneath the northern East Pacific Rise. *Nature*, *495*(7442), 499–502.

Key, K. (2016). MARE2DEM: a 2-D inversion code for controlled-source electromagnetic and magnetotelluric data. *Geophysical Journal International*, *207*(1), 571–588.

Khan, A. (2016). On Earth's mantle constitution and structure from joint analysis of geophysical and laboratory-based data: An example. *Surveys in Geophysics*, *37*(1), 149–189.

Kohlstedt, D. L., & Mackwell, S. J. (1998). Diffusion of Hydrogen and Intrinsic Point Defects in Olivine. *Zeitschrift Für Physikalische Chemie*, 207, 147–162.

Laumonier, M., Gaillard, F., & Sifre, D. (2015). The effect of pressure and water concentration on the electrical conductivity of dacitic melts: Implication for magnetotelluric imaging in subduction areas. *Chemical Geology*, *418*, 66–76.

Laumonier, M., Farla, R., Frost, D. J., Katsura, T., Marquardt, K., Bouvier, A. S., & Baumgartner, L. P. (2017). Experimental determination of melt interconnectivity and electrical conductivity in the upper mantle. *Earth and Planetary Science Letters*, *463*, 286–297.

Li, Z.-X. A., Lee, C.-T. A., Peslier, A. H., Lenardic, A., & Mackwell, S. J. (2008). Water contents in mantle xenoliths from the Colorado Plateau and vicinity: Implications for the mantle rheology and hydration-induced thinning of continental lithosphere. *J. Geophys. Res.*, *113*, B09210.

Libowitzky, E., & Rossman, G. R. (1996). Principles of quantitative absorbance measurements in anisotropic crystals. *Physics and Chemistry of Minerals*, *23*(6), 319–327.

Liu, L., & Hasterok, D. (2016). High-resolution lithosphere viscosity and dynamics revealed by magnetotelluric imaging. *Science*, *353*(6307), 1515–1519.

Marquardt, K., Rohrer, G. S., Morales, L., Rybacki, E., Marquardt, H., & Lin, B. (2015). The most frequent interfaces in olivine aggregates: the GBCD and its importance for grain boundary related processes. *Contributions to Mineralogy and Petrology*, 170(4), 40.

McHone, J.G. (2000). Non-plume magmatism and rifting during the opening of the central Atlantic Ocean. *Tectonophysics*, 316(3–4), 287–296.

Meqbel, N.M., Egbert, G.D., Wannamaker, P.E., Kelbert, A. and Schultz, A. (2014). Deep electrical resistivity structure of the northwestern US derived from 3-D inversion of USArray magnetotelluric data. *Earth and Planetary Science Letters*, *402*, 290-304.

McGary, R. S., Evans, R. L., Wannamaker, P. E., Elsenbeck, J., & Rondenay, S. (2014). Pathway from subducting slab to surface for melt and fluids beneath Mount Rainier. *Nature*, *511*(7509), 338–340.

Miller, K. J., Montési, L. G., & Zhu, W. (2015). Estimates of olivine–basaltic melt electrical conductivity using a digital rock physics approach. *Earth and Planetary Science Letters*, *432*, 332–341.

Misener, D. J. (1974). Cationic diffusion in olivine to 1400°C and 35 kbar, in *Geochemical Transport and Kinetics*, edited by A. W. Hofmann et al., 117–129, Carnegie Institution of Washington, Washington, D. C.

Mott, N. F., & Gurney, R. W. (1948). Ch 2 in *Electronic processes in ionic crystals*, 2nd edn. Oxford University Press, Oxford.

Müller, A., & Haak, V. (2004). 3-D modeling of the deep electrical conductivity of Merapi volcano (Central Java): integrating magnetotellurics, induction vectors and the effects of steep topography. *Journal of volcanology and geothermal research*, *138*(3-4), 205–222.

Murphy, B. S., & Egbert, G. D. (2017). Electrical conductivity structure of southeastern North America: Implications for lithospheric architecture and Appalachian topographic rejuvenation. *Earth and Planetary Science Letters*, 462, 66–75.

Murphy, B. S., & Egbert, G. D. (2018). Source biases in midlatitude magnetotelluric transfer functions due to Pc3-4 geomagnetic pulsations. *Earth, Planets and Space*, *70*(1), 12.

Murphy, B.S., Egbert, G. (2019). Synthesizing Seemingly Contradictory Seismic and Magnetotelluric Observations in the Southeastern United States to Image Physical Properties of the Lithosphere. *Geochemistry, Geophysics, Geosystems*, 20(6), 2606–2625.

Naif, S., Key, K., Constable, S., & Evans, R. L. (2013). Melt-rich channel observed at the lithosphere-asthenosphere boundary. *Nature*, 495(7441), 356–359.

Naif, S., Key, K., Constable, S., & Evans, R. L. (2015). Water-rich bending faults at the Middle America Trench. *Geochemistry Geophysics Geosystems*, 16(8), 2582–2597.

Naif, S. (2018). An upper bound on the electrical conductivity of hydrated oceanic mantle at the onset of dehydration melting. *Earth and Planetary Science Letters*, 482, 357–366.

Nesbitt, B. E. (1993). Electrical resistivities of crustal fluids. *Journal of Geophysical Research: Solid Earth*, *98*(B3), 4301–4310.

Ni, H., Keppler, H., & Behrens, H. (2011). Electrical conductivity of hydrous basaltic melts: implications for partial melting in the upper mantle. *Contributions to Mineralogy and Petrology*, *162*(3), 637–650.

Ni, H., Hui, H., & Steinle-Neumann, G. (2015). Transport properties of silicate melts. *Reviews of Geophysics*, *53*(3), 715–744.

Novella, D., Jacobsen, B., Weber, P. K., Tyburczy, J. A., Ryerson, F. J., & Frane, Du, W. L. (2017). Hydrogen self-diffusion in single crystal olivine and electrical conductivity of the Earth's mantle. *Scientific Reports*, 7(1).

1587 O'Leary, J. A., Gaetani, G. A., & Hauri, E. H. (2010). The effect of tetrahedral Al3+ on the
1588 partitioning of water between clinopyroxene and silicate melt. *Earth and Planetary Science*
1589 *Letters*, *297*(1-2), 111–120.

1590 Özaydın, S., & Selway, K. (2020). MATE: An Analysis Tool for the Interpretation of
1591 Magnetotelluric Models of the Mantle. *Geochemistry, Geophysics, Geosystems*, *21*(9),
1592 e2020GC009126.

1593 Padilha, A.L., Vitorello, Í., Pádua, M.B. and Bologna, M.S. (2006). Lithospheric and
1594 sublithospheric anisotropy beneath central-southeastern Brazil constrained by long period
1595 magnetotelluric data. *Physics of the Earth and Planetary Interiors*, *158*(2–4), 190–209.

1596 Paterson, M. (1982). The determination of hydroxyl by infrared absorption in quartz,
1597 silicate glasses and similar materials. *Bulletin de minéralogie*, *105*(1), 20–29.

1598 Peacock, J. R., & Selway, K. (2016). Magnetotelluric investigation of the Vestfold Hills and
1599 Rauer Group, East Antarctica. *Journal of Geophysical Research: Solid Earth*, *121*(4), 2258–
1600 2273.

1601 Persikov, E. S., Bukhtiyarov, P. G., & Sokol, A. G. (2017). Viscosity of hydrous kimberlite and
1602 basaltic melts at high pressures. *Russian Geology and Geophysics*, *58*(9), 1093–1100.

1603 Poe, B. T., Romano, C., Nestola, F., & Smyth, J. R. (2010). Electrical conductivity anisotropy of
1604 dry and hydrous olivine at 8GPa. *Physics of the Earth and Planetary Interiors, 181(3–4)*,
1605 103–111.

1606 Pollitz, F. F., & Mooney, W. D. (2016). Seismic velocity structure of the crust and shallow
1607 mantle of the Central and Eastern United States by seismic surface wave imaging.
1608 *Geophysical Research Letters*, 43, 118–126.

1609 Pommier, A., Gaillard, F., Malki, M., & Pichavant, M. (2010). Methodological re-evaluation of
1610 the electrical conductivity of silicate melts. *American Mineralogist*, *95*(2-3), 284–291.

1611 Pommier, A., Evans, R. L., Key, K., Tyburczy, J. A., Mackwell, S., & Elsenbeck, J. (2013).
1612 Prediction of silicate melt viscosity from electrical conductivity: A model and its
1613 geophysical implications. *Geochemistry, Geophysics, Geosystems*, *14*(6), 1685–1692.

1614 Pommier, A. (2014). Interpretation of magnetotelluric results using laboratory
1615 measurements. *Surveys in Geophysics*, *35*(1), 41–84.

1616 Pommier, A., Leinenweber, K., Kohlstedt, D. L., Qi, C., Garnero, E. J., Mackwell, S. J., &
1617 Tyburczy, J. A. (2015). Experimental constraints on the electrical anisotropy of the
1618 lithosphere–asthenosphere system. *Nature*, *522*(7555), 202–206.

1619 Pommier, A., Kohlstedt, D. L., Hansen, L. N., Mackwell, S., Tasaka, M., Heidelbach, F., &
1620 Leinenweber, K. (2018). Transport properties of olivine grain boundaries from electrical
1621 conductivity experiments. *Contributions to Mineralogy and Petrology*, *173*(5), 41.

Quist, A. S., & Marshall, W. L. (1968). Electrical conductances of aqueous sodium chloride solutions from 0 to 800 degrees and at pressures to 4000 bars. *The Journal of Physical Chemistry*, *72*(2), 684–703.

Rai, C. S., & Manghnani, M. H. (1977). Electrical conductivity of basalts to 1550C. In: Dick, H.J.B. (Ed.), *Magma Genesis Bull. 96,* Oregon Dept. Geol. Miner. Ind., Portland, pp. 219–237.

Reynes, J., Jollands, M., Hermann, J., & Ireland, T. (2018). Experimental constraints on hydrogen diffusion in garnet. *Contributions to Mineralogy and Petrology, 173(69)*.

Roberts, J. J., & Tyburczy, J. A. (1991). Frequency dependent electrical properties of polycrystalline olivine compacts. *Journal of Geophysical Research: Solid Earth*, *96*(B10), 16205–16222.

Roberts, J. J., & Tyburczy, J. A. (1993). Impedance Spectroscopy of Single and Polycrystalline Olivine: Evidence for Grain Boundary Transport. *Physics and chemistry of minerals*, *20*, 19–26.

Robertson, K., Heinson, G., & Thiel, S. (2016). Lithospheric reworking at the Proterozoic–Phanerozoic transition of Australia imaged using AusLAMP Magnetotelluric data. *Earth and Planetary Science Letters*, *452*, 27–35.

Robertson, K., Thiel, S., & Meqbel, N. (2020). Quality over quantity: on workflow and model space exploration of 3D inversion of MT data. *Earth, Planets and Space*, *72*(1), 1–22.

Rodi, W. L., & Mackie, R. L. (2012). The inverse problem. *The Magnetotelluric Method: Theory and Practice*, 347–414.

Romano, C., Poe, B. T., Kreidie, N., & McCammon, C. A. (2006). Electrical conductivities of pyrope-almandine garnets up to 19 GPa and 1700 C. *American Mineralogist*, *91*(8–9), 1371–1377.

Saal, A. E., Hauri, E. H., Langmuir, C. H., & Perfit, M. R. (2002). Vapour undersaturation in primitive mid-ocean-ridge basalt and the volatile content of Earth's upper mantle. *Nature*, *419*(6906), 451–455.

Sappa, G., Ergul, S., & Ferranti, F. (2014). Water quality assessment of carbonate aquifers in southern Latium region, Central Italy: a case study for irrigation and drinking purposes. *Appl Water Sci*, *4*, 115–128.

Sarafian, E., Evans, R. L., Collins, J. A., Elsenbeck, J., Gaetani, G. A., Gaherty, J. B., Hirth, G., & Lizarralde, D. (2015). The electrical structure of the central Pacific upper mantle constrained by the NoMelt experiment. *Geochemistry, Geophysics, Geosystems*, *16*(4), 1115–1132.

Schlechter, E., Stalder, R., & Behrens, H. (2012). Electrical conductivity of H-bearing orthopyroxene single crystals measured with impedance spectroscopy. *Physics and Chemistry of Minerals*, *39*(7), 531–541.

Schmandt, B., & Lin, F.-C. (2014). P and S wave tomography of the mantle beneath the United States. *Geophysical Research Letters*, 41, 6342–6349.

Schock, R. N. & Duba, A. G. (1985). Points Defects and the Mechanisms of Electrical Conduction in Olivine. *Point Defects in Minerals*, 88–96.

Schock, R. N., Duba, A. G., & Shankland, T. J. (1989). Electrical conduction in olivine. *Journal of Geophysical Research, 94(B5)*, 5829–5839.

Seifert, K.F., Will, G., & Voigt, R. (1982) Electrical conductivity measurements on synthetic pyroxenes MgSiO3-FeSiO3 at high pressures and temperatures under defined thermodynamic conditions. In W. Schreyer, Ed., *High-pressure Researches in Geoscience*, 419–432. Schweizerbart'sche, Stuttgart.

Selway, K. (2015). Negligible effect of hydrogen content on plate strength in East Africa. *Nature Geoscience*, *8*(7), 543–546.

Selway, K., Ford, H. and Kelemen, P. (2015). The seismic mid-lithosphere discontinuity. *Earth and Planetary Science Letters*, *414*, 45–57.

Selway, K. (2018). Electrical discontinuities in the continental lithosphere imaged with magnetotellurics. *Lithospheric Discontinuities*, 89–109.

Selway, K., & O'Donnell, J. P. (2019). A small, unextractable melt fraction as the cause for the low velocity zone. *Earth and Planetary Science Letters*, *517*, 117–124.

Selway, K., O'Donnell, J. P., & Özaydin, S. (2019). Upper mantle melt distribution from petrologically constrained magnetotellurics. *Geochemistry, Geophysics, Geosystems*, *20*(7), 3328–3346.

Selway, K., Smirnov, M. Y., Beka, T., O'Donnell, J. P., Minakov, A., Senger, K., ... & Kalscheuer, T. (2020). Magnetotelluric Constraints on the Temperature, Composition, Partial Melt Content, and Viscosity of the Upper Mantle Beneath Svalbard. *Geochemistry, Geophysics, Geosystems*, *21*(5), e2020GC008985.

Shankland, T. J., & Duba, A. G. (1990). Standard electrical conductivity of isotropic, homogeneous olivine in the temperature range 1200–1500 C. *Geophysical Journal International*, *103*(1), 25–31.

Shellnutt, J. G., Dostal, J., & Yeh, M. W. (2018). Mantle source heterogeneity of the Early Jurassic basalt of eastern North America. *International Journal of Earth Sciences*, *107*(3), 1033–1058.

1689 Sifré, D., Gardés, E., Massuyeau, M., Hashim, L., Hier-Majumder, S., & Gaillard, F. (2014).
1690 Electrical conductivity during incipient melting in the oceanic low-velocity
1691 zone. *Nature*, *509*(7498), 81–85.

1692 Sim, S. J., Spiegelman, M., Stegman, D. R., & Wilson, C. (2020). The influence of spreading
1693 rate and permeability on melt focusing beneath mid-ocean ridges. *Physics of the Earth and*
1694 *Planetary Interiors*, *304*, 106486.

1695 Simpson, F., & Bahr, K. (2005). *Practical magnetotellurics*. Cambridge University Press.

1696 Singh, D. K., Singh, R. P., & Kamra, A. K. (2004). The electrical environment of the Earth's
1697 atmosphere: A review. *Space Science Reviews*, *113*(3), 375–408.

1698 Sinmyo, R., & Keppler, H. (2017). Electrical conductivity of NaCl-bearing aqueous fluids to
1699 600° C and 1 GPa. *Contributions to Mineralogy and Petrology*, *172*(1), 4.

1700 Siripunvaraporn, W., Egbert, G., Lenbury, Y., & Uyeshima, M. (2005). Three-dimensional
1701 magnetotelluric inversion: data-space method. *Physics of the Earth and Planetary*
1702 *Interiors*, *150*(1-3), 3–14.

1703 Smyth, D. M., & Stocker, R. L. (1975). Point defects and non-stoichiometry in
1704 forsterite. *Physics of the Earth and Planetary Interiors*, *10*(2), 183–192.

1705 Stachel, T., Brey, G. P., & Harris, J. W. (2005). Inclusions in sublithospheric diamonds:
1706 glimpses of deep Earth. *Elements*, *1*(2), 73–78.

1707 Sun, W., Yoshino, T., Kuroda, M., Sakamoto, N., & Yurimoto, H. (2019). H–D interdiffusion in
1708 single crystal olivine: implications for electrical conductivity in the upper mantle. *Journal of*
1709 *Geophysical Research: Solid Earth*, 2019JB017576–12.

1710 Ten Grotenhuis, S. M., Drury, M. R., Spiers, C. J., & Peach, C. J. (2005). Melt distribution in
1711 olivine rocks based on electrical conductivity measurements. *Journal of Geophysical*
1712 *Research: Solid Earth*, *110*(B12).

1713 Thiel, S., Heinson, G. and White, A. (2005). Tectonic evolution of the southern Gawler
1714 Craton, South Australia, from electromagnetic sounding. *Australian Journal of Earth*
1715 *Sciences*, *52*(6), 887–896.

1716 Tyburczy, J. A., & Waff, H. S. (1983). Electrical conductivity of molten basalt and andesite to
1717 25 kilobars pressure: Geophysical significance and implications for charge transport and
1718 melt structure. *Journal of Geophysical Research*, 88(B3), 2413–2430.

1719 Tyburczy, J. A., & Fisler, D. K. (1995). Electrical properties of minerals and melts. *Mineral*
1720 *physics and crystallography, a handbook of physical constants*, 185–208.

1721 Vozoff, K. (1991). The magnetotelluric method. In *Electromagnetic Methods in Applied*
1722 *Geophysics: Volume 2, Application, Parts A and B* (pp. 641-712). Society of Exploration
1723 Geophysicists.

Wagner, L. S., Fischer, K. M., Hawman, R., Hopper, E., & Howell, D. (2018). The relative roles of inheritance and long-term passive margin lithospheric evolution on the modern structure and tectonic activity in the southeastern United States. *Geosphere*, 14(4), 1385–1410.

Wang, D., Mookherjee, M., Xu, Y., & Karato, S.-i. (2006). The effect of water on the electrical conductivity of olivine. *Nature*, 443(7114), 977–980.

Wang, D., Li, H., Yi, L., Matsuzaki, T. and Yoshino, T. (2010). Anisotropy of synthetic quartz electrical conductivity at high pressure and temperature. *Journal of Geophysical Research: Solid Earth*, *115*(B9).

Wang, D., Guo, Y., Yu, Y. and Karato, S.I. (2012). Electrical conductivity of amphibole-bearing rocks: influence of dehydration. *Contributions to Mineralogy and Petrology*, *164*(1), 17–25.

Wannamaker, P. E. (2000). Comment on "The petrologic case for a dry lower crust" by Bruce WD Yardley and John W. Valley. *Journal of Geophysical Research: Solid Earth*, *105*(B3), 6057–6064.

Wannamaker, P. E., Hasterok, D. P., Johnston, J. M., Stodt, J. A., Hall, D. B., Sodergren, T. L., et al. (2008). Lithospheric dismemberment and magmatic processes of the Great Basin–Colorado Plateau transition, Utah, implied from magnetotellurics. *Geochemistry, Geophysics, Geosystems*, *9*(5).

Wannamaker, P., Hill, G., Stodt, J., Maris, V., Ogawa, Y., Selway, K., Boren, G., Bertrand, E., Uhlmann, D., Ayling, B. and Green, A.M. (2017). Uplift of the central transantarctic mountains. *Nature communications*, *8*(1).

Watson, B. (2002). Mobility of siderophile elements in grain boundaries of periclase and periclase/olivine aggregates. AGU-SM, 2002, V52B-05.

Waxman, M. H., & Smits, L. J. M. (1968). Electrical conductivities in oil-bearing shaly sands. *Society of Petroleum Engineers Journal*, *8*(02), 107–122.

Whalen, L., Gazel, E., Vidito, C., Puffer, J., Bizimis, M., Henika, W., and Caddick, M. J. (2015). Supercontinental inheritance and its influence on supercontinental breakup: The Central Atlantic Magmatic Province and the break up of Pangea, *Geochem. Geophys. Geosyst.*, 16, 3532–3554. doi:10.1002/2015GC005885.

White, R. S., McKenzie, D., & O'Nions, R. K. (1992). Oceanic crustal thickness from seismic measurements and rare earth element inversions. *Journal of Geophysical Research: Solid Earth*, *97*(B13), 19683–19715.

Whittall, K. P., & Oldenburg, D. W. (1992). *Inversion of magnetotelluric data for a one-dimensional conductivity*. Society of Exploration Geophysicists.

Wilson, C. R., Spiegelman, M., van Keken, P. E., & Hacker, B. R. (2014). Fluid flow in subduction zones: The role of solid rheology and compaction pressure. *Earth and Planetary Science Letters*, *401*, 261–274.

Worzewski, T., Jegen, M., Kopp, H., Brasse, H., & Castillo, W. T. (2011). Magnetotelluric image of the fluid cycle in the Costa Rican subduction zone. *Nature Geoscience*, *4*(2), 108–111.

Wunderman, R. L., Wannamaker, P. E., & Young, C. T. (2018). Architecture of the hidden Penokean terrane suture and Midcontinent rift system overprint in eastern Minnesota and western Wisconsin from magnetotelluric profiling. *Lithosphere*, *10*(2), 291–300.

Xu, Y., Shankland, T. J. & Duba, A. G. (2000). Pressure effect on electrical conductivity of mantle olivine. *Physics of the Earth and Planetary Interiors*, *118*, 149–161.

Xu, Y., Zhang, A., Yang, B., Bao, X., Wang, Q., Xia, J., & Yang, W. (2018). Bridging the connection between effective viscosity and electrical conductivity through water content in the upper mantle. *Scientific reports*, *8*(1), 1–8.

Yang, B., Egbert, G.D., Kelbert, A. and Meqbel, N.M. (2015). Three-dimensional electrical resistivity of the north-central USA from EarthScope long period magnetotelluric data. *Earth and Planetary Science Letters*, *422*, 87–93.

Yang, X., Keppler, H., McCammon, C., Ni, H., Xia, Q. and Fan, Q. (2011). Effect of water on the electrical conductivity of lower crustal clinopyroxene. *Journal of Geophysical Research: Solid Earth*, *116*(B4).

Yang, X., Keppler, H., McCammon, C. and Ni, H. (2012). Electrical conductivity of orthopyroxene and plagioclase in the lower crust. *Contributions to Mineralogy and Petrology*, *163*(1), 33-48.

Yardley, B. W., & Valley, J. W. (1997). The petrologic case for a dry lower crust. *Journal of Geophysical Research: Solid Earth*, *102*(B6), 12173–12185.

Yardley, B. W. D., & Valley, J. W. (2000). Reply [to "Comment on 'The petrologic case for a dry lower crust'by Bruce WD Yardley and John W. Valley"]. *Journal of Geophysical Research: Solid Earth*, *105*(B3), 6065–6068.

Yoshino, T., Matsuzaki, T., Yamashita, S., & Katsura, T. (2006). Hydrous olivine unable to account for conductivity anomaly at the top of the asthenosphere. *Nature*, *443*(7114), 973–976.

Yoshino, T., Matsuzaki, T., Shatskiy, A., & Katsura, T. (2009). The effect of water on the electrical conductivity of olivine aggregates and its implications for the electrical structure of the upper mantle. *Earth and Planetary Science Letters*, *288(*1-2), 291–300.

Yoshino, T., & Katsura, T. (2009). Effect of iron content on electrical conductivity of ringwoodite, with implications for electrical structure in the transition zone. *Physics of the Earth and Planetary Interiors*, *174*(1-4), 3–9.

Yoshino, T. (2010). Laboratory Electrical Conductivity Measurement of Mantle Minerals. *Surveys in Geophysics*, 31(2), 163–206.

Yoshino, T., Laumonier, M., McIsaac, E., & Katsura, T. (2010). Electrical conductivity of basaltic and carbonatite melt-bearing peridotites at high pressures: implications for melt distribution and melt fraction in the upper mantle. *Earth and Planetary Science Letters*, *295*, 593–602.

Yoshino, T., & Katsura, T. (2013). Electrical Conductivity of Mantle Minerals: Role of Water in Conductivity Anomalies. *Annual Review of Earth and Planetary Sciences*, *41*(1), 605–628.

Yoshino, T., Zhang, B., Rhymer, B., Zhao, C., & Fei, H. (2017). Pressure dependence of electrical conductivity in forsterite. *Journal of Geophysical Research: Solid Earth, 122(1)*, 158–171.

Yoshino, T. (2018). Electrical Conductivity Measurement. In *Magmas Under Pressure* (pp. 281–319). Elsevier. http://doi.org/10.1016/B978-0-12-811301-1.00011-3

Zhang, B., Yoshino, T., Wu, X., Matsuzaki, T., & Shan, S. (2012). Electrical conductivity of enstatite as a function of water content: Implications for the electrical structure in the upper mantle. *Earth and Planetary Science Letters*, 447, 1–9.

Zhang, B., Yoshino, T., Yamazaki, D., Manthilake, G., & Katsura, T. (2014). Electrical conductivity anisotropy in partially molten peridotite under shear deformation. *Earth and Planetary Science Letters*, *405*, 98–109.

Zhao, C., & Yoshino, T. (2016). Electrical conductivity of mantle clinopyroxene as a function of water content and its implication on electrical structure of uppermost mantle. *Earth and Planetary Science Letters*, 447, 1–9.

Zhu, W., Gaetani, G. A., Fusseis, F., Montési, L. G., & De Carlo, F. (2011). Microtomography of partially molten rocks: three-dimensional melt distribution in mantle peridotite. *Science*, *332*(6025), 88–91.